Geoscience Frontiers 14 (2023) 101537

HOSTED BY

Contents lists available at ScienceDirect

Geoscience Frontiers

journal homepage: www.elsevier.com/locate/gsf

Research Paper

Roller-coaster atmospheric-terrestrial-oceanic-climatic system during Ordovician-Silurian transition: Consequences of large igneous provinces

Licai Song [a,b,c], Qing Chen [d], Huijun Li [b], Changzhou Deng [c,*]

[a] School of Earth Sciences and Resources, China University of Geosciences (Beijing), Beijing 100083, China
[b] Key Laboratory of Paleomagnetism and Tectonic Reconstruction, Institute of Geomechanics, Chinese Academy of Geological Sciences, China Geological Survey, Ministry of Natural Resources, Beijing 100081, China
[c] State Key Laboratory of Ore Deposit Geochemistry, Institute of Geochemistry, Chinese Academy of Sciences, Guiyang 550081, China
[d] State Key Laboratory of Palaeobiology and Stratigraphy, Nanjing Institute of Geology and Palaeontology and Center for Excellence in Life and Palaeoenvironment, Chinese Academy of Sciences, Nanjing 210008, China

ARTICLE INFO

Article history:
Received 26 May 2022
Revised 24 December 2022
Accepted 14 January 2023
Available online 18 January 2023
Handling Editor: V.O. Samuel

Keywords:
Earth system
Large igneous province
Mercury isotope
Late Ordovician mass extinction
Phosphorus recycling

ABSTRACT

The Ordovician-Silurian transition (OST) hosted profound and frequent changes in the atmospheric-terres trial-oceanic-climatic system (ATOCS). Previous studies have found contrasting stages for such changes, primarily based on hiatus-interrupted sections. However, the dominant driving factors and mechanisms reconciling such frequent changes remain controversial. Mercury isotopes, which undergo both mass-dependent and mass-independent fractionation, can provide critical insights into the deep-time ATOCSs, especially for those impacted by large igneous provinces (LIPs) events. Here, we build a high-resolution multi-proxy record of Hg (concentrations and isotopic compositions) combined with organic carbon isotopes ($\delta^{13}C_{org}$) and whole-rock geochemical data (including trace elements and phosphorus) from continuous cores in the Yangtze Platform, South China. Our data, combined with reported ones, indicate the occurrence of LIP eruptions against localized volcanism, and four successive, yet contrasting stages of ATOCSs during the OST. Moreover, we identified the coupling between two-pulse LIP magmatism and extreme ATOCSs, each with special pCO_2, weathering rate, primary productivity, redox condition, climatic mode, and biotic evolution. For stage I, the first pulse of LIP magmatism triggered global warming, enhanced terrestrial weathering, oceanic acidification, eutrophication, anoxia, P recycling, and thereby widespread deposition of black shales. During stage II, the Hirnantian glaciation and oxygenation arose from the intense chemical weathering and black shale deposition of stage I; slashed terrestrial weathering and oceanic oxygenation facilitated CO_2 accumulation. In stage III, another pulse of LIP magmatism triggered the de-glaciation, and the ATOCS was largely similar to that of stage I. This led to another round of oxygenation and positive $\delta^{13}C_{org}$ excursion in stage IV. Compared with the environmental pressure by the peculiar ATOCS of each stage, their transitions might have been more devastating in triggering the prolonged Late Ordovician Mass Extinction (LOME). Moreover, limited biotic recovery was possible in the later portion of stages I and III. The multi-proxy study of continuous strata of the OST provides an excellent framework for better illuminating LIPs' essential role in driving the "roller-coaster" behavior of the ATOCS and thus biotic crisis during the pivotal period of the OST.

1. Introduction

Frequent and profound changes occurred in the atmospheric-t errestrial-oceanic-climatic system (ATOCS) during the Ordovician-Silurian transition (from 449.13 Ma to 439.43 Ma) (Gradstein et al., 2020) (Fig. 1). Such changes include fluctuations of atmospheric CO_2 levels (Lenton et al., 2018), low but rising atmospheric O_2 levels (Brand et al., 2021), origination and expansion of the earliest land plants (Lenton et al., 2012), sea-level fluctuations (Li et al., 2021), oceanic anoxic events (OAEs) (Melchin et al., 2013; Stockey et al., 2020), the Hirnantian glaciation (Finnegan et al., 2011), and, most noticeably, Late Ordovician mass extinction (LOME) (Sheehan, 2001) (Fig. 1).

As the first of the "Big Five" mass extinctions, the LOME has long been the focus of research on the ATOCS during the

* Corresponding author.
E-mail address: dengchangzhou@mail.gyig.ac.cn (C. Deng).

https://doi.org/10.1016/j.gsf.2023.101537

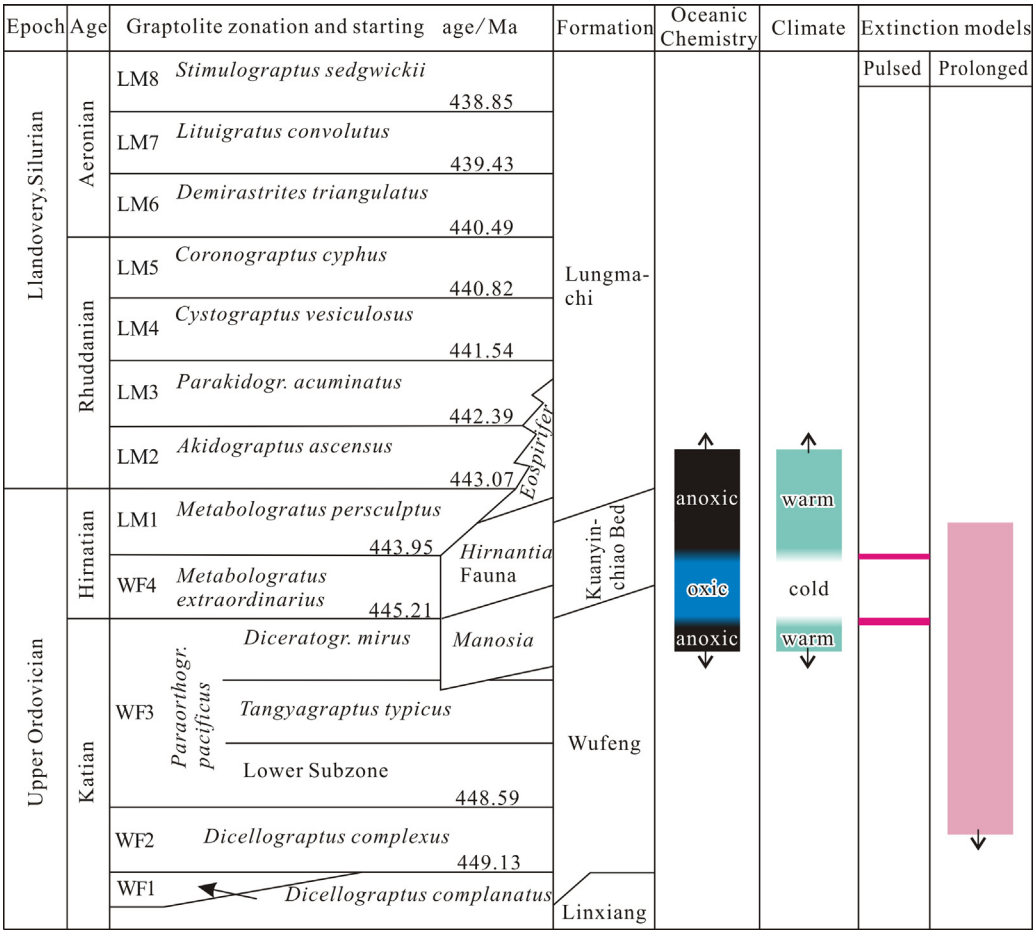

Fig. 1. Biological and lithological divisions of sedimentary strata during the Ordovician-Silurian transition in the Yangtze Platform, South China. Graptolite zonation and corresponding abbreviations after Chen et al. (2015) and their starting ages after Gradstein et al. (2020), ocean chemistry and climate changes after Wang et al. (2019), extinction models after Fan et al. (2020).

Ordovician-Silurian transition (Sheehan, 2001; Harper et al., 2014; Fan et al., 2020). Various hypotheses of the ATOCS have been proposed based on the swift, two- or single-pulse models of extinction, centering on the Hirnantian glaciation and OAEs (Wang et al., 2019; Bond and Grasby, 2020; Gradstein et al., 2020). However, recent high-resolution analyses of paleontological data have challenged such swift models of extinction (Rasmussen et al., 2019; Fan et al., 2020). Thus, the causal mechanism in the ATOCS for the LOME remains enigmatic.

Geochemical studies on strata of the Ordovician-Silurian transition used to be relatively rare (Melchin et al., 2013), especially on continuously deposited outcrops or cores (Calner et al., 2021; Li et al., 2021). China's shale gas exploitation has inspired intense investigations on the continuous strata of the Ordovician-Silurian transition in the Yangtze Platform, South China (Ma et al., 2018) (Figs. 1 and 2). Previous studies have proposed that localized factors prevailed in the deposition of the black organic-rich graptolitic shales ("black shales" for short), including semi-enclosed paleogeography (Chen et al., 2004) and localized volcanism (Zhao et al., 2020; Du et al., 2021). However, these black shales belong to the first in time and second in scale of the six Phanerozoic global-scale petroleum source rock black shales (Klemme and Ulmishek, 1991; Arthur and Sageman, 1994), indicating ubiquitous OAEs along the northern margin of Gondwana at that time (Melchin et al., 2013). The Ordovician-Silurian OAEs are remarkably more protracted than the Mesozoic OAEs (Bartlett et al., 2018; Stockey et al., 2020; Dahl et al., 2021). Moreover, the positive feedback between the OAEs and the recycling of phosphorus (P) (Schobben et al., 2020) during the Ordovician-Silurian transition has been barely touched.

Global changes in the ATOCS can be recorded by isotopic carbon excursions (ICEs), which indicate major perturbations in the global carbon cycle (Jenkyns, 2010; Black and Gibson, 2019). Remarkably positive ICEs have been documented accompanying the roller-coaster ATOCS (Bergström and Goldman, 2019). Over geological time, volcanism-related carbon is the principal input for CO_2 in the atmospheric-terrestrial-oceanic system (McKenzie and Jiang, 2019), and large igneous provinces (LIPs) can release voluminous CO_2 in geologically short duration (often < 2 Myr) or multiple discrete shorter pulses through a longer period (Kasbohm et al., 2021). Flood basalts and (ultra)mafic intrusions are among the most remarkable records of LIPs, upon which intensified chemical weathering and enhanced oceanic productivity effectively enhance CO_2 sequestration as negative feedback on the sharp CO_2 inputs (Kasbohm et al., 2021; Torsvik et al., 2021). Therefore, LIPs have long been linked with geologically rapid ATOCS changes (Kasbohm, 2022). However, such volcanic inputs cannot be detected or identified solely by the carbon isotope records (Black and Gibson, 2019; Schobben et al., 2019). Moreover, the poor radiogenic isotope geochronology of the late Katian-Hirnantian

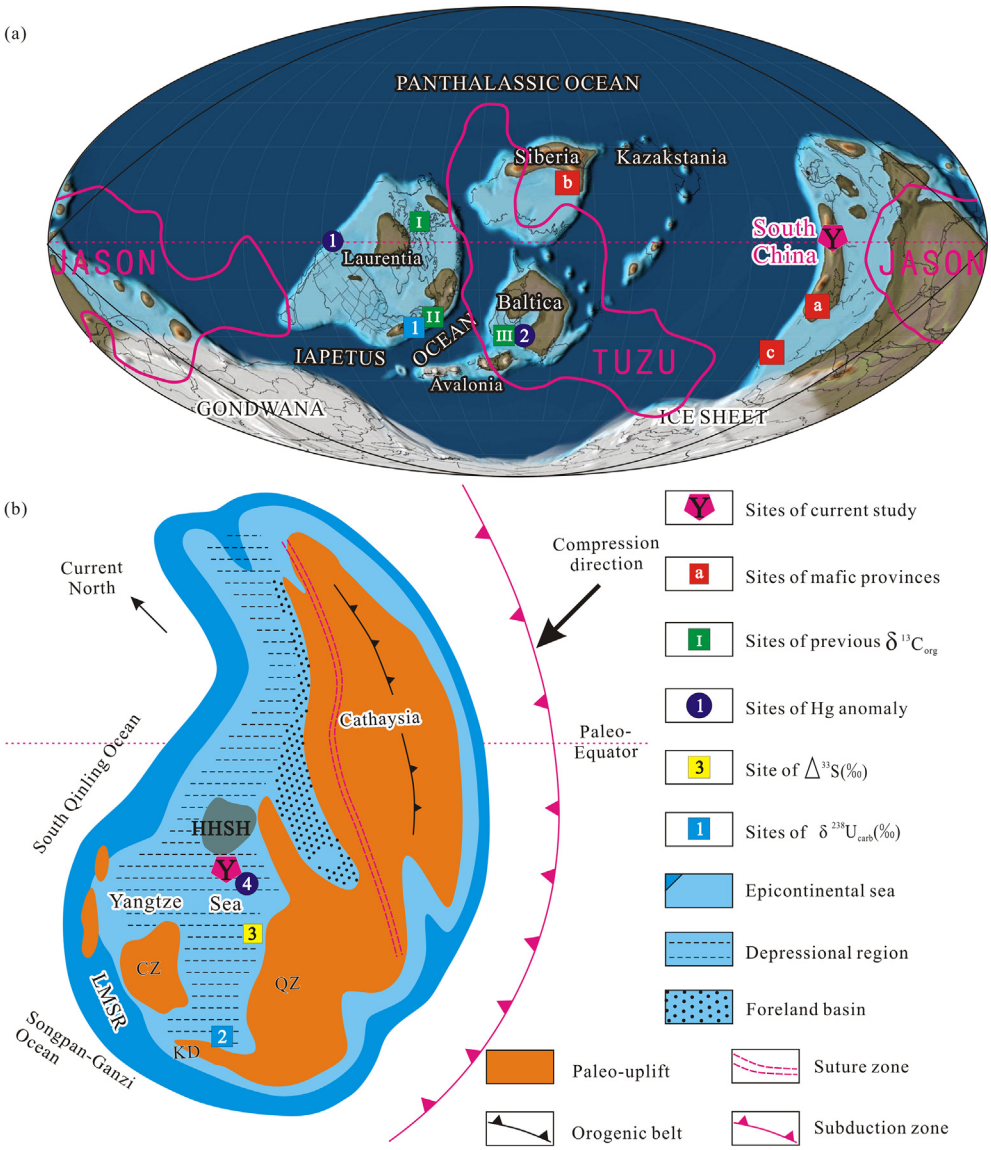

Fig. 2. Paleogeography of the globe (a, after Scotese et al. (2021)) and South China (b, after Chen et al. (2004)) during the Hirnantian stage, Ordovician. Abbreviations: CZ, Chuanzhong Uplift; K_D, Kangdian Palaeo-high; LMSR, Longmenshan Rift; QZ, Qianzhong Uplift; HHSH, Hunan-Hubei Subwater High. "TUZU" and "JASON" are two large low shear-wave velocity provinces in the deepest mantle (Torsvik et al., 2021).

sequences poses great difficulties in matching LIPs with the profound ATOCS and biological changes (Torsvik et al., 2021) and further challenges the LIPs as the trigger for such changes.

Therefore, albeit the close temporal coincidence and possible interconnections among the changes in the ATOCS, the dominant driving factors and mechanisms reconciling such changes are still controversial. Sedimentary mercury enrichment and isotopic characteristics are "smoking guns" for LIPs, and allow for direct correlation with concomitant geological records (Grasby et al., 2019; Yager et al., 2021; Nauter-Alves, 2022), thereby providing a unique opportunity for exploring the ATOCS during the Ordovician-Silurian transition.

Recent studies have observed high Hg anomalies near the Ordovician-Silurian boundary, and proposed the immediate environmental deterioration by LIP eruption as the primary trigger for the swift, two- or single-pulse models of LOME (Gong et al., 2017; Smolarek-Lach et al., 2019; Hu et al., 2021) (Fig. 2). The contributions of Hg enrichment by pyrites were also explored (Shen et al., 2019; Shen et al., 2022a). However, to illuminate the cause-and-effect relationships between LIPs and successive stages of the ATOCSs and their transitions in the Ordovician-Silurian transition, as well as the interactions among the ATOCS, an integration of data of multiple proxies that are well-constrained by graptolite biostratigraphy remains lacking.

Successive strata spanning the Ordovician-Silurian transition are well-developed and preserved in the Yangtze Platform, South China, and serve as commercial shale gas reservoirs (Ma et al., 2018). Generalized graptolite zonation of these strata enables a remarkably higher-resolution division than U-Pb geochronology can do (Chen et al., 2015; Gradstein et al., 2020) (Fig. 1). Thanks to the plausibility of the global correlation of both the graptolite zonation (Chen et al., 2015; Gradstein et al., 2020) and the strata themselves (Arthur and Sageman, 1994; Chen et al., 2015), a unique opportunity exists for exploring the changes in the ATOCS and their driving mechanisms from a global perspective.

Here, we present the first high-resolution multi-proxy record of Hg (concentrations and isotopic compositions), organic carbon isotopes ($\delta^{13}C_{org}$), and whole-rock geochemical data (including trace

elements and P) from a continuous shale gas well core (Y#) that is calibrated by graptolite biostratigraphy from the Yangtze Platform (Fig. 2). We integrate our data with previously published ones to investigate the possible coupling relationships between the pulses of LIP magmatism and the fluctuations in oceanic redox, productivity, P recycling, and C cycling. Besides the temporal correlation of pulsed LIP magmatism and the ATOCS, we further analyze the feedback loops among them to test the causal connections. Our study explores the driving role of LIP magmatism on the roller-coaster ATOCS during the Ordovician-Silurian transition from a global view and attempts to raise attention to similar variations in other geological periods.

2. Geological background

During the Ordovician-Silurian transition, Gondwana occupied the southern hemisphere and the Panthalassa Ocean covered most of the northern hemisphere. South China, along with Laurentia, Baltica, Avalonia, and Siberia, was located to the north of Gondwana and transected by the equator (Scotese, 2021) (Fig. 2a). The Yangtze Platform of South China was half-surrounded by several paleo-uplifts, with an opening to the South Qinling Ocean in the north (Chen et al., 2004) (Fig. 2b). In many parts of the Yangtze Platform, continuous strata were deposited spanning the Ordovician-Silurian transition (Chen et al., 2015).

Four successive, but lithologically distinct, stages at the Ordovician-Silurian transition have been identified in the Yangtze Platform (Figs. 1 and 3): (1) black shales of the Ordovician Wufeng Formation, coinciding with graptolite zones of *Dicellograptus complexus* (WF2), *Paraothograptus pacificus* (WF3) and the lowermost *Metabogograptus extraordinarius* (WF4); (2) argillaceous limestones and calcareous mudstones of the Ordovician Kuanyinchiao Bed, characteristic of *Hirnatia* fauna and corresponding to graptolite zones of middle and upper WF4 and lower *Metabolograptus persculptus* (LM1); (3) black shales of the Lungmachi Formation, correlating with graptolite zones of upper LM1 and upwards to *Cystograptus vesiculosus* (LM4); and (4) silty shales of the Silurian Lungmachi Formation, corresponding to graptolite zones of *Coronograptus cyphus* (LM5) and upwards (Chen et al., 2015).

Such a four-stage division is common in many contemporaneous sections and cores from the Yangtze platform (Chen et al., 2015; Ma et al., 2018), including Well Y# (Fig. 3) in this study. This division is also applicable in many other parts of the world (Melchin et al., 2013; Štorch et al., 2018). These black shales belong to the first in time and second in spatial distribution of the six sets of Phanerozoic petroleum source rocks at the global scale (Arthur and Sageman, 1994), and are indicators of OAEs that are more prolonged than the Mesozoic OAEs (Jenkyns, 2010; Melchin et al., 2013; Dahl et al., 2021). The interbedded Kuanyinchiao bed correlates with the glacial deposits on the Gondwanan continent, indicating the Hirnantian glaciation (Melchin et al., 2013).

Well Y# is a new shale gas well from China's main shale gas productivity zones in the Yangtze Platform, with continuously drilled cores spanning the Ordovician-Silurian transition. Its depositional environment was the inner shelf near the depositional center of the Yangtze Platform (Chen et al., 2004) (Fig. 2b).

3. Samples and methods

Twenty-two samples were collected from Well Y# (Fig. 3). The samples were cleaned with 18.2 MΩ·cm water, air-dried, powdered using an agate mortar and pestle, passed through a 200 mesh sieve, and homogenized for chemical analyses.

Measurements of the TOC concentration (wt.%) followed the Walkley-Black procedure (Gelman et al., 2012) at the Institute of Geochemistry, Chinese Academy of Sciences, which yielded a relative standard deviation of < 5% for duplicate samples. Organic carbon isotopes ($\delta^{13}C_{org}$) were analyzed at the Ministry Key Laboratory of Metallogeny and Mineral Assessment, China, using a MAT 253 isotope-ratio mass spectrometer. The results were calibrated by USGS40 ($\delta^{13}C$ = −26.39‰) and UREA ($\delta^{13}C$ = −37.32‰) and presented in per-mil (‰) relative to the V-PDB standard (Qi et al., 2003; Schimmelmann et al., 2016). The analytical precision of $\delta^{13}C_{org}$ was better than ± 0.1‰.

Major- and trace-element concentrations were acquired at the National Engineering Research Center for Comprehensive Utilization of Non-metallic Mineral Resources, China, using X-ray fluorescence and inductively coupled plasma-mass spectrometry, with analytical uncertainty of < ±5% and < ±10%, respectively. Redox-sensitive and organic matter-related trace element concentrations were normalized and translated as enrichment factors (EF) (EF-Mo and EF-Cu) to better illuminate the paleo-redox conditions and

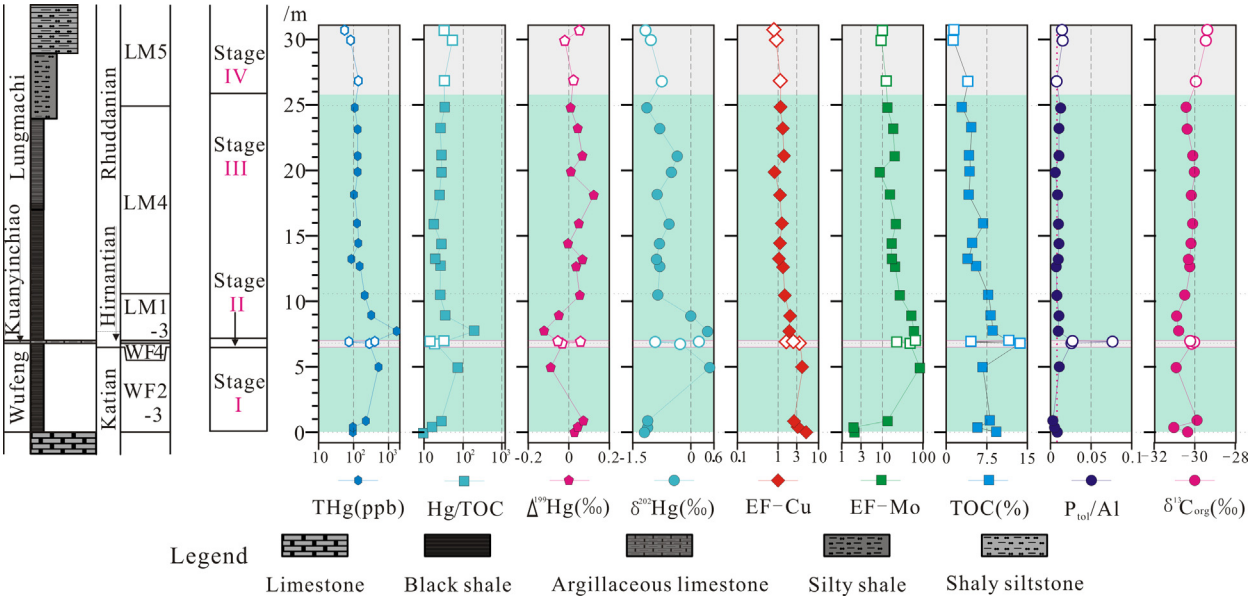

Fig. 3. Geochemical plots for Well Y# across the Ordovician-Silurian boundary. Refer to Fig. 1 for abbreviations for graptolite zonation.

paleo-productivity (Tribovillard et al., 2006; Algeo and Rowe, 2012; Algeo and Liu, 2020; Tribovillard, 2021). EF is calculated using the following equation:

$$EF-X=(X/Al)_{sample}/(X/Al)_{PAAS} \quad (1)$$

where X is either Cu or Mo; $(X/Al)_{sample}$ and $(X/Al)_{PAAS}$ are Al-normalized X concentrations in the sample and the post-Archean Australian shale, respectively (Taylor and McLennan, 1985).

Mercury concentrations were determined by a DMA-80 direct Hg analyzer at the Institute of Geochemistry, Chinese Academy of Sciences. Measurement of standard reference material (GSS-4, soil) yielded Hg recoveries of 90% – 110%, and the relative standard deviations of sample duplicates were all within 10%. Mercury isotopes were analyzed by Neptune Plus multi-collector inductively coupled plasma mass spectrometry at the same institute (Yin et al., 2016). Mass-dependent fractionation of Hg isotopes (Hg-MDF) is expressed in δ^{202}Hg notation in units of per-mil (‰) referenced to the NIST-3133 Hg standard (analyzed before and after each sample):

$$\delta^{202}Hg(‰)=[(^{202}Hg/^{198}Hg_{sample})/(^{202}Hg/^{198}Hg_{standard})-1]\times 1000 \quad (2)$$

Mass-independent fractionation of Hg isotopes (Hg-MIF) is reported in Δ notation (Δ^{xxx}Hg), which describes the difference between the measured δ^{xxx}Hg. It is calculated using the following formula:

$$\Delta^{xxx}Hg \approx \delta^{xxx}Hg - \delta^{202}Hg \times \beta \quad (3)$$

where β is equal to 0.2520, 0.5024, and 0.7520 for ^{199}Hg, ^{200}Hg, and ^{201}Hg, respectively (Blum and Bergquist, 2007). Analytical uncertainty was estimated based on the replicates of the NIST 3177 secondary standard solution and full procedural analyses of GSS-4. The overall average and uncertainty of NIST-3177 (δ^{202}Hg: −0.52‰ ± 0.08‰; Δ^{199}Hg: 0 ± 0.05‰; Δ^{201}Hg: 0 ± 0.06‰; 2SD, n = 11) and GSS-4 (δ^{202}Hg: −1.63‰ ± 0.11‰; Δ^{199}Hg: −0.41‰ ± 0.05‰; Δ^{201}Hg: −0.43‰ ± 0.06‰; 2SD, n = 5) agree well with previous results (Blum and Bergquist, 2007; Deng et al., 2021a). Uncertainties reported in this study correspond to the larger value of either (1) the uncertainty of replicate analysis of GSS-4, or (2) the uncertainty of repeated measurements of NIST-3177.

4. Results

According to the analytical results of this study (Supplementary Data Tables S1-S3), four stages can be identified in Well Y# throughout the Ordovician-Silurian transition, as illustrated in Fig. 3. Samples from stage I show elevated values of EF-Cu (2.52 to 5.14), EF-Mo (1.94 to 84.73), TOC (5.88–9.31 wt.%), THg (93.5–501.2 ppb), and Hg/TOC (10.0–72.9 ppb/wt.%). $\delta^{13}C_{org}$ possesses consistently negative values of −31.0‰ to −29.9‰. In stage I, δ^{202}Hg values (−1.21‰ to 0.50‰) increase from the bottom to the top, whereas Δ^{199}Hg values (−0.09‰ to 0.07‰) exhibit an opposite pattern. In stage I, the P_{tol}/Al values are very small (0.003 to 0.011).

In stage II, dramatic decreases in EF-Cu (1.69), EF-Mo (23.10), TOC (4.78 wt.%), THg (72.2), and Hg/TOC(15.1 ppb/wt.%) are present. While $\delta^{13}C_{org}$ and Δ^{199}Hg display large positive excursions (−30.0‰ and 0.06‰, respectively), δ^{202}Hg shows a negative excursion (−0.92‰). In stage II, the P_{tol}/Al values yield a spike of 0.077.

Near the bottom of stage III, high values of EF-Cu (1.51 to 2.02), EF-Mo (27.21 to 60.91), TOC (7.93–8.72 wt.%), THg (203.9–1727.3 ppb), and Hg/TOC (25.7–198.1 ppb/wt.%) can be observed, associated with decreases in $\delta^{13}C_{org}$ (−30.9‰) and Δ^{199}Hg (−0.12‰) but increases in δ^{202}Hg (0.45‰). The middle and upper parts of stage III display small variations in EF-Cu (0.85 to 1.43), EF-Mo (13.60 to 21.63), TOC (4.18–7.05 wt.%), THg (85.0–152.9 ppb), Hg/TOC (18.1–34.3 ppb/wt.%), $\delta^{13}C_{org}$ (−30.4‰ to −30.0‰), δ^{202}Hg (−1.13‰ to −0.35‰) and Δ^{199}Hg (0.01‰ – 0.12‰). The P_{tol}/Al ratios resume small values (0.006 to 0.012).

Samples in stage IV possess similar values to the upper parts of state III, including EF-Cu (0.84 to 1.21), EF-Mo (9.71 to 12.41), Hg/TOC (32.9–53.5 ppb/wt.%), δ^{202}Hg (−1.17‰ to −0.75‰), and Δ^{199}Hg (−0.02‰ – 0.05‰). In the meantime, they yield slightly positive $\delta^{13}C_{org}$ (−29.9‰ to −29.3‰) values, and lower THg (55.2–140.0 ppb) and TOC (1.51–4.21 wt.%) levels. The P_{tol}/Al values display a small increase (0.008 to 0.015).

5. Discussion

5.1. Successive yet distinctive stages of the ATOCS during the Ordovician-Silurian transition

5.1.1. Stage I: Anoxic and warm

Stage I is represented by the black shales of stage I. It spans the graptolite zones of WF2 to the lowermost WF4, roughly from 449.13 Ma to 445.21 Ma of the middle and late Katian (Chen et al., 2015; Gradstein et al., 2020) (Figs. 1 and 3). The black shales of stage I in Well Y# correlate well with many contemporaneous sections and cores from the Yangtze Platform, China (Chen et al., 2015; Ma et al., 2018), and many other parts of the world (Melchin et al., 2013; Štorch et al., 2018) (Fig. 4a).

Some trace elements (e.g., Cu) are mainly transferred to the sediments by organic matter fluxes and can be retained within pyrites after the partial decomposition of organic matter (Raiswell et al., 2018; Algeo and Liu, 2020; Tribovillard, 2021). Their enrichments in marine sediments (e.g., EF-Cu) are robust proxies of oceanic primary productivity (Algeo and Li, 2020; Algeo and Liu, 2020; Tribovillard, 2021). Therefore, the elevated EF-Cu and TOC values in the black shales of stage I (Fig. 3) indicate high oceanic primary productivity. Our data of small P_{tol}/Al values approaching the average shale reference value of 0.008 (Schobben et al., 2020) also suggest a minimal burial of P against the high primary productivity (Figs. 3 and 4b).

Some other trace elements (e.g., Mo) are redox-sensitive and tend to enrich in deposits from anoxic water columns (Algeo and Li, 2020; Algeo and Liu, 2020; Tribovillard, 2021). Therefore, the elevated EF-Mo values in the black shales of stage I (Fig. 3) indicate the anoxia of bottom waters. Moreover, global marine anoxia tracers (δ^{98}Mo, δ^{238}U) from both shales and carbonate rocks across South China, Laurentia, and Baltica point to widespread anoxia (Chen et al., 2021; Dahl et al., 2021; Liu et al., 2022) (Fig. 4b). Notably, the high-resolution constraint on the duration of such anoxia (Figs. 1 and 4b) demonstrates that it is much longer than the Mesozoic oceanic anoxic events (Jenkyns, 2010).

Besides the aforementioned proxies, although we did not acquire suitable samples for oxygen isotope analysis, estimates of sea surface temperatures by oxygen isotope paleothermometry (Finnegan et al., 2011; Männik et al., 2021; Marcilly et al., 2022) indicate a warm state. Additionally, chemical index of alteration (CIA) data in South China (Yan et al., 2010) and Tarim (Zhang et al., 2021), and lithium isotopes (δ^{7}Li) in Laurentia (Pogge von Strandmann et al., 2017) also signify intensified terrestrial weathering during stage I.

Therefore, our data, combined with previously reported ones, demonstrate that, the ocean, especially the epicontinental portion, was characteristic of widespread high primary productivity and bottom water anoxia during stage I. The climate was warm then. Also, terrestrial chemical weathering was relatively intense. These different aspects of the ATOCS exhibit coordination as discussed below.

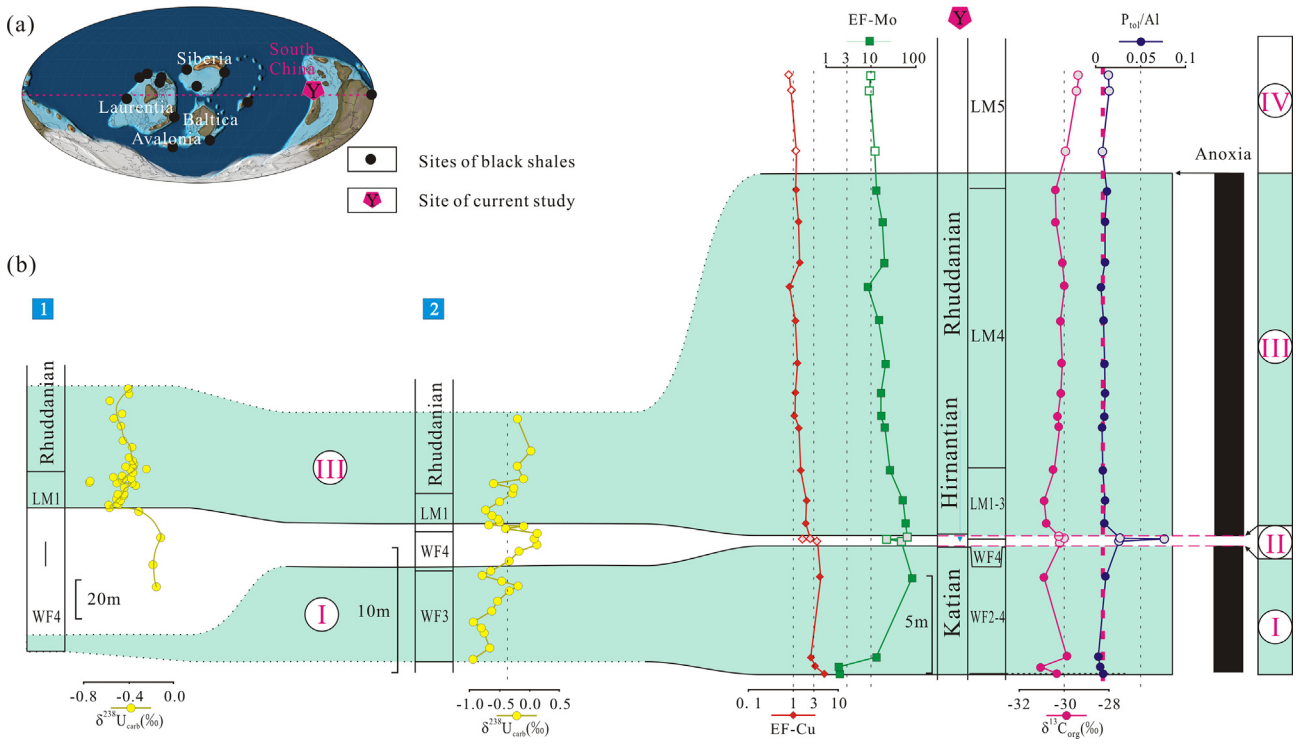

Fig. 4. Transcontinental correlation of geochemical data for oceanic redox changes around the Ordovician-Silurian transition. Locations of U isotopes are shown in Fig. 2: '1', western Anticosti Island section, Quebec, Canada, Laurentia (Bartlett et al., 2018); '2', Wuke section, South China (Liu et al., 2022); Sites of black shales deposition during both Interval I and III are after Melchin et al. (2013), base map is the same as Fig. 2. See Fig. 1 for abbreviations for graptolite zonation.

Terrestrial weathering under a warm state can effectively transfer the bio-essential trace elements and P to the ocean, facilitating oceanic primary productivity (Hartmann et al., 2014; Horton, 2015). With much lower than the present-day atmospheric O_2 content (16.2% ± 1.2% (Brand et al., 2021)), the marine dissolved O_2 would be correspondingly lower in the Katian Age. High oceanic primary productivity would increase organic matter shuttle to the seafloor and thus O_2 demand; subsequently, this leads to O_2 depletion of bottom water and the ultimate global anoxia or euxinia, or at least in the vast platforms or epicontinental seas (Meyer and Kump, 2008; Piper and Calvert, 2009). Minimal burial of P against high primary productivity might be the result of P recycling. This is because P tends to be released from the organic-carbon-rich sediments and shuttled upwards under anoxic/euxinic bottom water columns (Schobben et al., 2020; Papadomanolaki et al., 2022). However, additional terrestrial input of nutrients is still necessary for sustaining high primary productivity and oceanic anoxic events (OAEs) over geologically long periods. Notably, such an OAE did not reach the photic zones since the graptolites were still abundant and evolved quickly during stage I (Chen et al., 2015).

5.1.2. Stage II: Glacial and oxic

Stage II is represented by the argillaceous limestones and calcareous mudstones of stage II, and covers the graptolite zones of middle and upper WF4 to lowermost LM1, approximately from 445.21 Ma to 443.95 Ma of the early Hirnantian (Chen et al., 2015; Gradstein et al., 2020) (Figs. 1 and 3).

The argillaceous limestones and calcareous mudstones of stage II of Well Y# belong to the relatively thin Kuanyinchiao Bed across the Yangtze Platform (Zhang et al., 2016) and coincide with many cool-water *Hirnantia* Fauna containing sections across different continents in the paleo-tropics (Melchin et al., 2013; Rong et al., 2020). Their contemporaneous strata also include the subtropical diamictites of Baltica (Porębski et al., 2019), widespread peri-Gondwanan glacial-related deposits of high latitudes (Delabroye and Vecoli, 2010), and carbonates overlain by unconformities (Brenchley et al., 2006; Ghienne et al., 2014; Calner et al., 2021).

The paleotropical cool-water *Hirnantia* Fauna and paleosubtropical and high-latitude glacial-related deposits indicate the climax of early Paleozoic cooling, and a global sea surface temperature plunge of about 5 to 7 °C during the Hirnantian glaciation (Trotter et al., 2008; Finnegan et al., 2011; Goldberg et al., 2021). Varying estimates of paleoatmospheric pCO_2 proposed a sharp decrease in pCO_2 to > 8 times preindustrial atmospheric levels (Gibbs et al., 1997; Herrmann et al., 2003), lower values of > 3 times (Pohl et al., 2016), or just a small drop in pCO_2 (Pohl et al., 2021). A recent study (Brand et al., 2021) inferred a rise in pO_2 that is coupled with the decline in pCO_2.

The low TOC values, alongside the reduced EF-Cu values, indicate low oceanic primary productivity (Fig. 3). In conjunction with their low-TOC correlatives in the Yangtze Platform and other continents, this suggests a widespread low primary productivity in the vast epicontinental seas during stage II (Melchin et al., 2013). Contrary to the low primary productivity, our data of elevated P contents (Figs. 3 and 4b), and phosphatic carbonates in Laurentia (Pope and Steffen, 2003) demonstrate widespread enrichment of P in sediments.

The low EF-Mo values reflect bottom water oxygenation (Fig. 3) and are consistent with the low TOC content in the strata. Moreover, such oxygenation is compatible with the coeval δ^{98}Mo and δ^{238}U excursions, indicative of widespread oxygenation spanning Laurentia and South China (Chen et al., 2021; Dahl et al., 2021; Liu et al., 2022) (Fig. 4b), and widespread distribution of aerobic benthic fauna (Rong et al., 2020; Zhang et al., 2022). Notably, stratigraphic iron speciation rarely reflects the redox of ancient water columns due to diagenetic and/or depositional influences (Pasquier et al., 2022) and sulfur isotopes of pyrites suffer from

strong local controls (Pasquier et al., 2021). Therefore, stratigraphic iron speciation and S isotopes of pyrites could mislead the interpretations of anoxia/euxinia (Hammarlund et al., 2012; Zou et al., 2018).

Evidence for weak terrestrial weathering comes from CIA data in South China (Yan et al., 2010) and δ^7Li data in Laurentia (Pogge von Strandmann et al., 2017). However, the terrestrial weathering of carbonates might be prominent, as evidenced by many unconformities underlain by the late Katian carbonates in South China, Laurentia, Baltica, and Avalonia (Kump et al., 1999; Kump and Arthur, 1999; Brenchley et al., 2006; Ghienne et al., 2014; Calner et al., 2021).

Stage II is also characterized by positive organic isotopic carbon excursion ($\delta^{13}C_{org}$), the Hirnantian ICE (HICE), which is the largest one in the Ordovician and has a good global correlation (Underwood et al., 1997; Melchin and Holmden, 2006a, 2006b; Edwards and Saltzman, 2016; Štorch et al., 2018; Hammarlund et al., 2019; Braun et al., 2021) (Fig. 5).

In brief, our data, and published ones together demonstrate that stage II is typical of low marine primary productivity, bottom water oxygenation, intense glaciation, and weak terrestrial weathering, while the burial of P was abnormally effective. These different aspects of the ATOCS can be explained as below.

Under the intense glaciation, terrestrial weathering was weak, and thus nutrient elements influx to the ocean was limited, resulting in low oceanic primary productivity. The low oceanic productivity would lead to low rates of organic matter shuttle to the seafloor, and correspondingly weak O_2 consumption in bottom water. P recycling would have been very low in such oxic conditions via the negative feedback of low primary productivity. The selective uptake and burial of $^{12}CO_2$ over $^{13}CO_2$ through the deposition of organic-carbon-rich shales during stage I (Saltzman and Young, 2005; Fan et al., 2009) might have contributed to the HICE. At the same time, the increased weathering of carbonates due to sea level fall would also supply isotopically heavier carbon (^{13}C) and thus favor the HICE (Kump and Arthur, 1999; Fan et al., 2009).

5.1.3. Stage III: Anoxic and warm

Stage III is represented by the black shales of stage III, and covers the graptolite zones of middle and upper LM1 to LM4, roughly from 443.95 Ma to 440.82 Ma of the late Hirnantian and early and middle Rhuddanian (Chen et al., 2015; Gradstein et al., 2020) (Figs. 1 and 3).

For this stage, the lithology and geochemical data of Y#, along with their coeval global correlatives, are broadly similar to those of stage I (Figs. 3–5). Therefore, the ATOCS and the feedback loops for both stages are similar to a large extent.

5.1.4. Stage IV: Cool and oxic

Stage IV is represented by the silty shales of stage IV. It corresponds to the graptolite zones of LM5, approximately from 443.82 Ma to 440.49 Ma of the latest Rhuddanian (Chen et al., 2015; Gradstein et al., 2020) (Figs. 1 and 3).

The characteristic silty shales for stage IV have transitional contact with the underlying black shales of stage III (Fig. 3), which is common not only in the Yangtze Platform of South China but also in many parts of the world (Melchin et al., 2013; Chen et al., 2015; Trela et al., 2016).

To some extent, the geochemical data of Y# for stage IV, as well as their coeval correlatives, are similar to those of stage II (Figs. 3–5). Correspondingly, the ATOCS and the feedback loops for both stages might also bear some similarities. Nonetheless, differences exist. For instance, during this stage, estimates based on oxygen isotope paleothermometry suggest a small-amplitude cooling. Ice

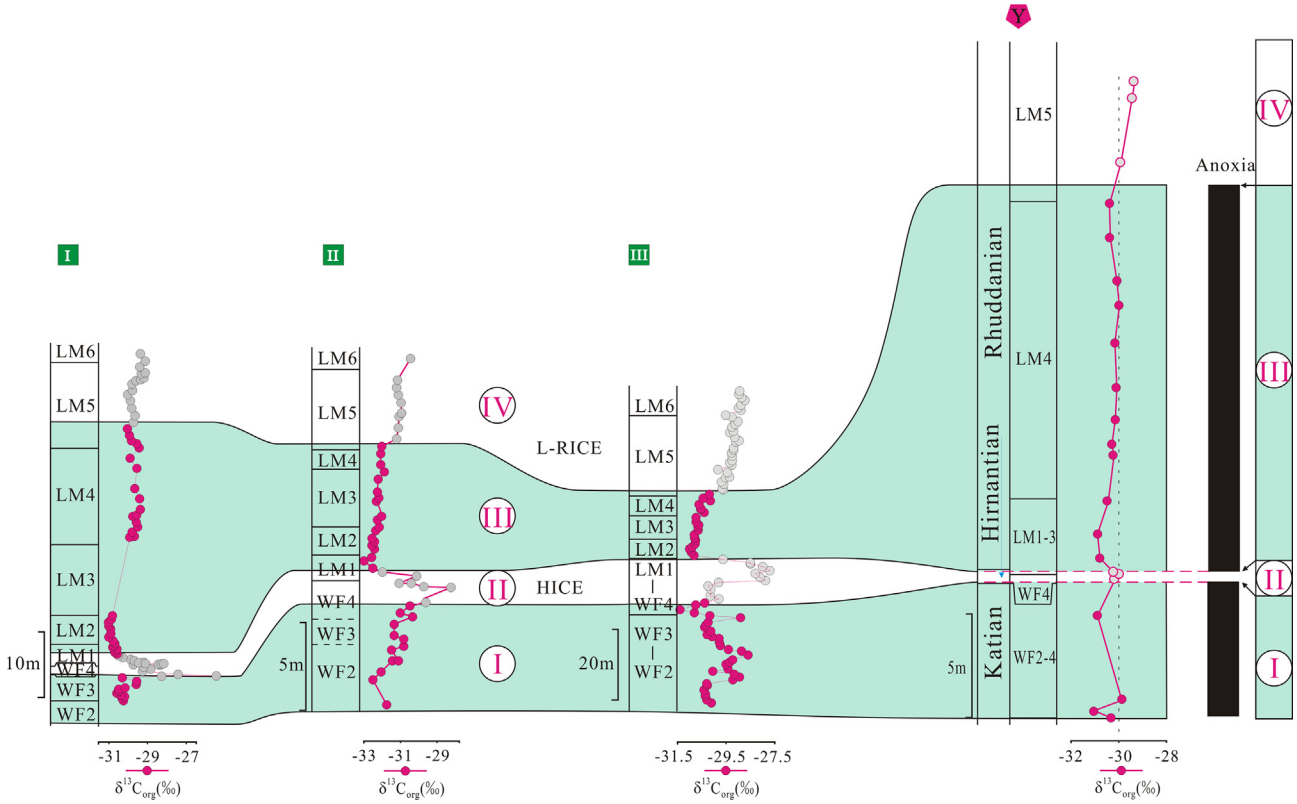

Fig. 5. Transcontinental correlation of geochemical data for organic carbon isotopes around the Ordovician-Silurian transition. Organic carbon isotopes' locations are in Fig. 2: 'I' for Cape Manning section, Arctic Canada, Laurentia (Melchin and Holmden, 2006a,b); 'II' for Dob's Linn section, Scotland, Laurentia (Underwood et al., 1997); 'III' for Sommerodde-1 core from Bornholm, Denmark, Baltica (Hammarlund et al., 2019). Refer to Fig. 1 for abbreviations for graptolite zonation.

sheets have also been reported (Finnegan et al., 2011; Melchin et al., 2013), although there has been no reported evidence for continental glaciation that is comparable to the Hirnantian glaciation.

Our $\delta^{13}C_{org}$ data and previously published results demonstrate the gradual occurrence of a low-amplitude, positive $\delta^{13}C_{org}$ excursion, in contrast to the sharp HICE (Fig. 5).

5.2. Issues and hints from sedimentary Hg records

5.2.1. Mechanism for swift starting and ending of the Hirnantian glaciation and prolonged LOME

As abovementioned, four successive yet distinct stages of the ATOCS alternated in a "roller-coaster" style during the Ordovician-Silurian transition (Fig. 6). The triggers for each stage of the ATOCS, and more intriguingly, the transition from one stage to the next, remain enigmatic. Notably, among these puzzles, the Hirnantian glaciation and the LOME are highly debated.

The cause for the Hirnantian glaciation remains poorly understood. Previous studies have proposed varying mechanisms in isolation for reducing atmospheric CO_2 (Pohl et al., 2021; Marcilly et al., 2022). These competing mechanisms include enhanced continental weathering by plants (Lenton et al., 2012; Porada et al., 2016) or by tectonic drifting/collision (Kump et al., 1999; Nardin et al., 2011; Swanson-Hysell and Macdonald, 2017), and organic carbon burial by eukaryotic bloom (Shen et al., 2018). However, such mechanisms are either inconsistent with geological records (Landing, 2018) or short of an explanation for the pCO_2 rise after the glaciation (Lenton et al., 2012).

As the first of the "Big Five" mass extinctions, the LOME has long been the focus of research on the ATOCS during the Ordovician-Silurian transition (Sheehan, 2001; Harper et al., 2014; Fan et al., 2020). The long-held models for LOME are the swift, two- or single-pulse models of extinction (Wang et al., 2019; Bond and Grasby, 2020; Gradstein et al., 2020) (Fig. 1). According to these swift models of extinction, stage II hosts the first and more severe strike of the LOME.

However, recent high-resolution analyses of paleontological data have demonstrated that the LOME might have been a prolonged biotic crisis, and stage I also hosts mass extinction (Rasmussen et al., 2019; Fan et al., 2020; Deng et al., 2021b) (Fig. 6).

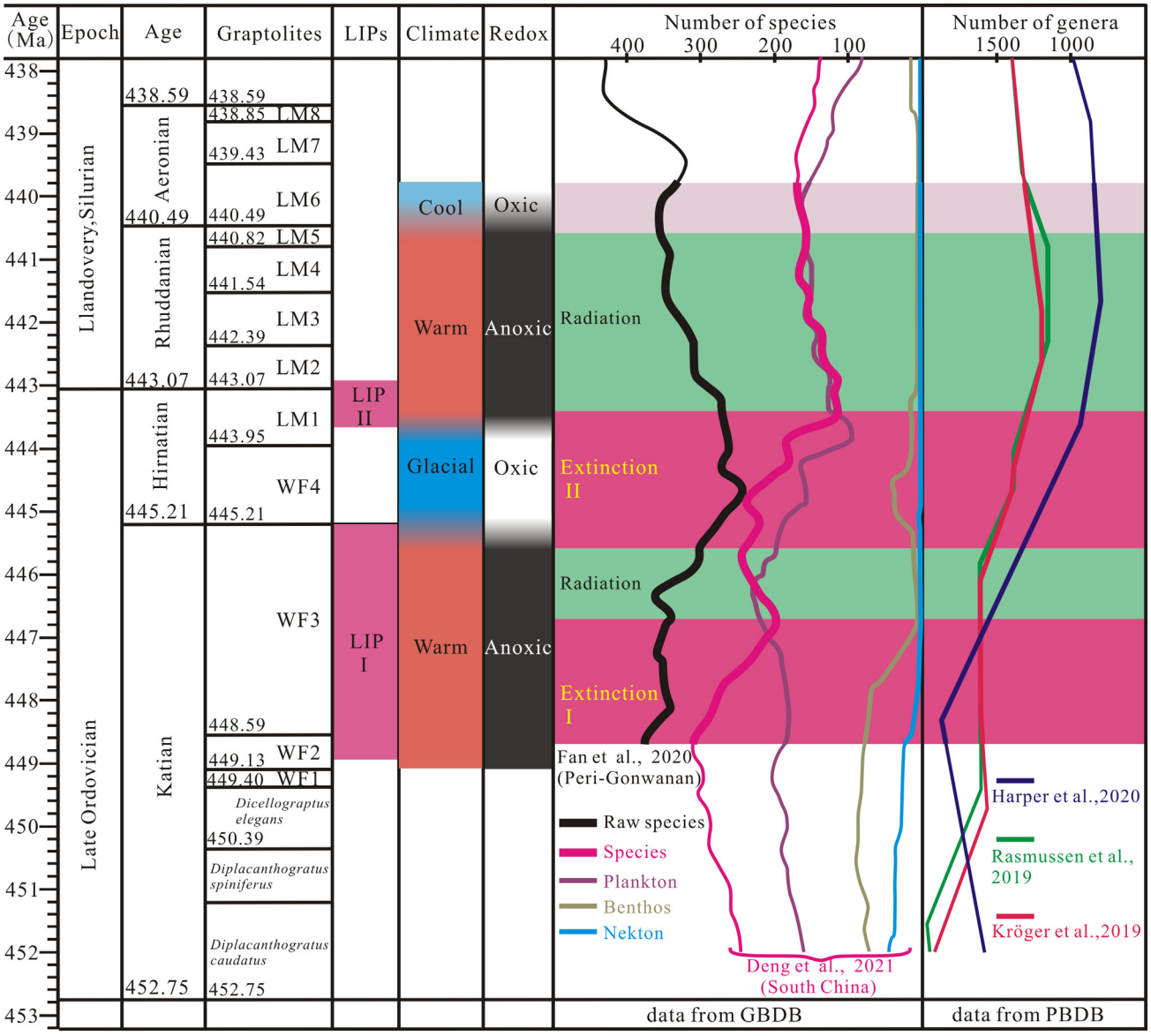

Fig. 6. Schematic diagram for the timeline of LIP magmatism, and climatic, oceanic, and biotic events around the Ordovician-Silurian transition. Biotic events are after Kröger et al. (2019), Rasmussen et al. (2019), Fan et al. (2020), Harper et al. (2020), Deng et al. (2021b). See Fig. 1 for abbreviations for graptolite zonation.

Contrary to stage I, much longer radiation succeeded the shorter extinction in stage III (Fig. 6). Widespread OAEs had long been attributed as a kill mechanism for the Phanerozoic mass extinctions, including the second, weaker pulse for LOME according to the swift, two-pulse model (Harper et al., 2014; Bond and Grasby, 2020; Liu et al., 2022). Notably, although the OAE spans the entire stage III, mass extinction occurred only in the very early portion of stage III (ending at 444.3 Ma, near the beginning of LM1), according to both the new prolonged extinction model (Rasmussen et al., 2019; Fan et al., 2020; Deng et al., 2021b) and the long-held swift, two-pulse model (Sheehan, 2001; Harper et al., 2014; Gradstein et al., 2020) (Figs. 1 and 6). Moreover, contrary to the extinction in stage II, only a minor break of post-LOME radiation in stage IV has been identified based on high-resolution analyses of paleontological data (Deng et al., 2021b) (Fig. 6). Therefore, the exact mechanism causing LOME remains unclear (Lindström et al., 2019; Fox et al., 2022).

Large igneous provinces (LIPs) have long been linked with geologically rapid changes in the ATOCS (Ernst et al., 2021; Torsvik et al., 2021; Kasbohm, 2022). They had also been hypothesized as the trigger for the Hirnantian glaciation by numerical modeling, yet no geological or geochemical evidence was provided (Lefebvre et al., 2010). Additionally, LIPs have also been accepted as a leading trigger for major Phanerozoic mass extinctions (Racki, 2020).

Furthermore, although precise isotopic dating ages are lacking, previous studies have proposed possible relics of LIPs at the Ordovician-Silurian transition (Kasbohm et al., 2021; Torsvik et al., 2021), for instance, the mafic igneous rocks in Korea of Sino-Korean Craton (445.0 ± 3.7 Ma and 452.5 ± 3.2 Ma) (Cho et al., 2014), Suordakh of Eastern Siberia Craton (458 ± 13 Ma) (Khudoley et al., 2020), and the Alborz LIP in northern Iran (443.7 ± 2.1 Ma) (Derakhshi et al., 2022) (Fig. 2a, sites of a-c). They were located nearly vertically above the margins of the large low shear-wave velocity provinces (namely, "TUZO" and "JASON"), which have been suggested to conform with the distribution of the past LIPs if their positions and shapes are largely unchanged (Torsvik et al., 2021) (Fig. 2a). Their dates might be highly valuable for tectonics, but higher-resolution dates are desired beforehand for scrutinizing the potential causal relationships between LIP magmatism and the ATOCS during the Ordovician-Silurian transition.

5.2.2. Sedimentary Hg with coeval correlatives spanning multiple continents and sedimentary environments within a biostratigraphic framework

Unlike the younger LIPs around the end-Permian and end-Triassic mass extinctions (Kasbohm et al., 2021), the lack of accessible rock records and methodological limitations prevent a comprehensive sample coverage and sufficiently high-precision radiometric dating of the candidate LIPs during the Ordovician-Silurian transition (Khudoley et al., 2020; Kasbohm et al., 2021). Furthermore, the relationships between LIPs and their downstream effects on ATOCS are not always uniform and straightforward (Ernst et al., 2021; Torsvik et al., 2021; Kasbohm, 2022). Therefore, higher-precision geochronology of the candidate LIPs (Khudoley et al., 2020; Ernst et al., 2021) in conjunction with the ATOCS records is still needed. Alternatively, comprehensive research by stratigraphic proxy records from the same successive stratigraphic sections is a key to exploring the overall timeline of LIPs' emplacement and the drastically fluctuating ATOCS and their causal connections.

LIPs can emit massive amounts of Hg into the environment, which is 10 to 10^3 times higher than normal levels (Grasby et al., 2020; Nauter-Alves, 2022). Mercury cycles in the atmospheric-terrestrial-oceanic ecosystem, and eventually enters the ocean via atmospheric Hg(II) deposition and terrestrial runoff (Blum et al., 2014). It is then delivered to the seabed via organic matter shuttle, and ultimately retained in organic matters (Grasby et al., 2019; Algeo and Liu, 2020; Yager et al., 2021) and authigenic sulfides after partial decay of the organic matters (Shen et al., 2019; Yager et al., 2021). Extensive studies on the end-Permian and end-Triassic mass extinctions have illustrated that the anomalously high Hg contents and Hg to total organic carbon (Hg/TOC) ratios are "smoking guns" for LIPs (Grasby et al., 2019; Percival et al., 2021; Yager et al., 2021; Nauter-Alves, 2022; Shen et al., 2022b).

Our sedimentary Hg data spanning the Ordovician-Silurian transition demonstrate anomalously high Hg concentrations and Hg/TOC ratios in the middle-upper stage I and the lowermost stage III (Figs. 3 and 7). Coeval enrichments of Hg (THg and/or Hg/TOC) have also been reported in Laurentia (Jones et al., 2017; Hu et al., 2021), Baltica (Smolarek-Lach et al., 2019; Bond and Grasby, 2020), and South China (Gong et al., 2017; Jones et al., 2017; Hu et al., 2021) (Fig. 2a and 7). Such enrichments of Hg can be well correlated with the biostratigraphy of graptolite zones (Fig. 7). The sedimentary environments of the Hg-hosting strata include the inner and middle epicontinental sea in South China (Hu et al., 2021), deep shelf facing the open sea in South China and Baltica (Gong et al., 2017; Jones et al., 2017; Smolarek-Lach et al., 2019), embayed carbonate platform margin in Laurentia (Jones et al., 2017), off-platform, and the deep sea around Laurentia and Baltica (Gong et al., 2017; Jones et al., 2017; Smolarek-Lach et al., 2019; Bond and Grasby, 2020; Hu et al., 2021). Indicators of remarkable sulfur-MIF anomalies for intense volcanism during the Ordovician-Silurian transition were also reported from South China (Hu et al., 2020) (Fig. 7). Therefore, two episodes of enrichments of Hg occurred not only in various sedimentary environments locally, but also at a global scale, or at least across multiple continents. The two pulses of enrichments of Hg spanning multiple continents are likely a marker of the pulsed LIP magmatism during the Ordovician-Silurian transition.

Additionally, for the enrichments of Hg in the Yangtze Platform, local influencing factors are also possible, including inputs of Hg by adjacent local-scale volcanism (Su et al., 2009; Yang et al., 2019; Du et al., 2021; Lu et al., 2022) and facilitation of burial by pyrites (Sanei et al., 2012; Shen et al., 2019). From a local perspective, the effects of local factors on the accumulation of Hg are still unclear and disputed (Percival et al., 2021). However, through the transcontinental correlation of Hg enrichments from different sedimentary environments, such local perturbations can be eliminated, since global driving mechanisms with overarching global impact are needed for the extensive Hg enrichment in both depositional environments and multi-continents during the Ordovician-Silurian transition. Moreover, the Ordovician-Silurian transition is one of the few periods with extensive records of Hg enrichment spanning different sedimentary environments across multiple continents (Percival et al., 2021). Therefore, it is highly likely that pulsed LIP magmatism is the predominant driver for the two pulses of Hg enrichments of stages I and III (Fig. 7).

Moreover, our data present negative mass-independent fractionation events of Hg (Hg-MIF, reported as Δ^{199}Hg) during both middle-upper stage I and lowermost stage III (Figs. 3 and 7). Hg-MIF occurs during photochemical processes with little contributions from other reactions (Blum et al., 2014; Deng et al., 2022). Photochemical processes can alter the isotope signature of volcanic Hg during its global cycling, resulting in positive Δ^{199}Hg in the atmospheric Hg(II) pool and negative Δ^{199}Hg in the gaseous Hg (0) pool (Bergquist and Blum, 2007). As terrestrial materials (soils and vegetation) receive Hg primarily through atmospheric Hg(0) deposition, they mainly show negative Δ^{199}Hg (Blum et al., 2014; Yin et al., 2022). Enrichments of Hg with near-zero Δ^{199}Hg were ascribed to an overwhelming influx of Hg by LIPs around the

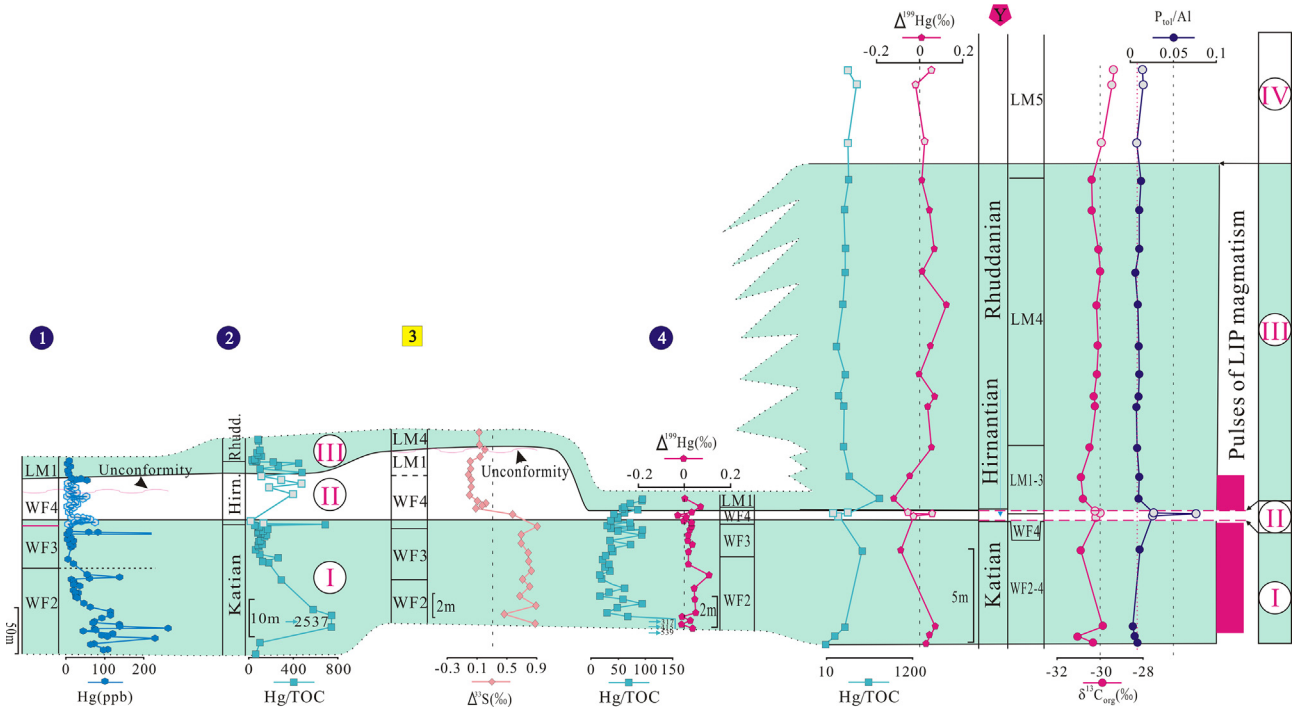

Fig. 7. Transcontinental correlation of geochemical proxies for LIPs around the Ordovician-Silurian transition. Hg enrichments' locations are in Fig. 2: '1′ for Monitor Range section, Nevada, USA, Laurentia (Jones et al., 2017), of which the unconformity is after Finney et al. (1999); '2′ for Zbrza PIG-1 borehole, Poland, Baltica (Smolarek-Lach et al., 2019); '3′ for XY5 borehole, South China (Hu et al., 2021). Sulphur isotope anomaly: '4′ for Honghuayuan section, South China (Hu et al., 2020), of which the unconformity is after Chen et al. (2017). Refer to Fig. 1 for abbreviations for graptolite zonation.

end-Triassic mass extinction (Thibodeau et al., 2016) and the LOME (Hu et al., 2021). However, further studies on the mercury records of LIPs during the end-Triassic, end-Permian, and end-Cretaceous reported negative Δ^{199}Hg from nearshore strata and/or positive Δ^{199}Hg from more distal and deepwater environments, demonstrating the durability of Hg-MIF pathways against the enormous Hg influx by LIPs (Grasby et al., 2019; Yager et al., 2021; Gu et al., 2022; Shen et al., 2022b). Therefore, our negative Hg-MIF data likely suggest the influences of Hg input associated with terrestrial soil erosion due to its location in the inner and middle epicontinental depositional environments (Grasby et al., 2019). Our data, along with the positive Hg-MIF in the deep shelf facing the open sea (Gong et al., 2017), provide a more detailed constraint on Hg cycling in the Yangtze Platform during the Ordovician-Silurian transition.

Therefore, we infer that two pulses of LIP magmatism occurred during the Ordovician-Silurian transition, based upon our data and their transcontinental correlatives within the high-resolution graptolite zonation (Fig. 7). We acknowledge that neither an unambiguous candidate LIP nor a stage-division of the ATOCS, with sufficiently high-resolution radiometric age constraints, is available so far.

5.3. Roller-coaster ATOCS driven by pulsed LIP magmatism during the Ordovician-Silurian transition

Although temporal coincidence has been proposed based on stratigraphic proxy records from the same successive stratigraphic section, LIP's driving role in the ATOCS requires further analyses on the feasibility of feedback loops among the ATOCS and pulsed LIP magmatism. This is because the scales and tempo of volatiles (Hg, SO_2, CO_2) and igneous rocks and their feedback in the ATOCS are always different (Ernst et al., 2021; Kasbohm et al., 2021; Torsvik et al., 2021; Kasbohm, 2022). Below we discuss the feedback loops from stage I to IV, with the main focus on the role of LIP magmatism in initiating and sustaining each stage.

5.3.1. Stage I with the first pulse of LIP magmatism

Besides Hg, LIPs can also release voluminous greenhouse gases (especially CO_2) and prodigious volumes of volcanic rocks and plume rocks (Black and Gibson, 2019; Black et al., 2021b; Ernst et al., 2021). Such an outburst of CO_2 is substantial enough to bring the Earth into a warm climate (Hull et al., 2020). Correspondingly, the terrestrial weathering would be intensified (Penman et al., 2020).

Moreover, recent high-resolution dating of the relatively young LIPs of the Columbia River Basalt Group, the Deccan Traps, and the Karoo-Ferrar LIP demonstrates that such global warming by CO_2 predated the basalt volcanism (Kasbohm et al., 2021; Gaynor et al., 2022; Tian and Buck, 2022). The nutrient-rich (especially P) pristine extrusive and plume rocks weather much faster than granitic rocks (Kump et al., 2000; Black et al., 2021a; Ernst et al., 2021). When they are exposed to the already warm climate, terrestrial chemical weathering is enhanced to even higher levels (Black et al., 2021a; Ernst et al., 2021; Kasbohm et al., 2021; Torsvik et al., 2021).

Such intensified terrestrial weathering tends to cause oceanic eutrophication and resultant anoxia/euxinia (Fig. 8), as evidenced by the Karoo-Ferrar LIP and Toarcian-OAE couplet (Heimdal et al., 2021; Gaynor et al., 2022). When such hostile conditions further deteriorated, mass extinction events occurred, as evidenced by the LIP-mass extinction couplets of the Deccan Traps with the end-Cretaceous extinction (Nava et al., 2021; Gu et al., 2022), the Central Atlantic Magmatic Province with the end-Triassic mass extinction (Yager et al., 2021), and the Siberian Traps with the end-Permian mass extinction (Schobben et al., 2020).

Therefore, in stage I, as inferred from our data and the transcontinental correlatives, the onset of high primary productivity and

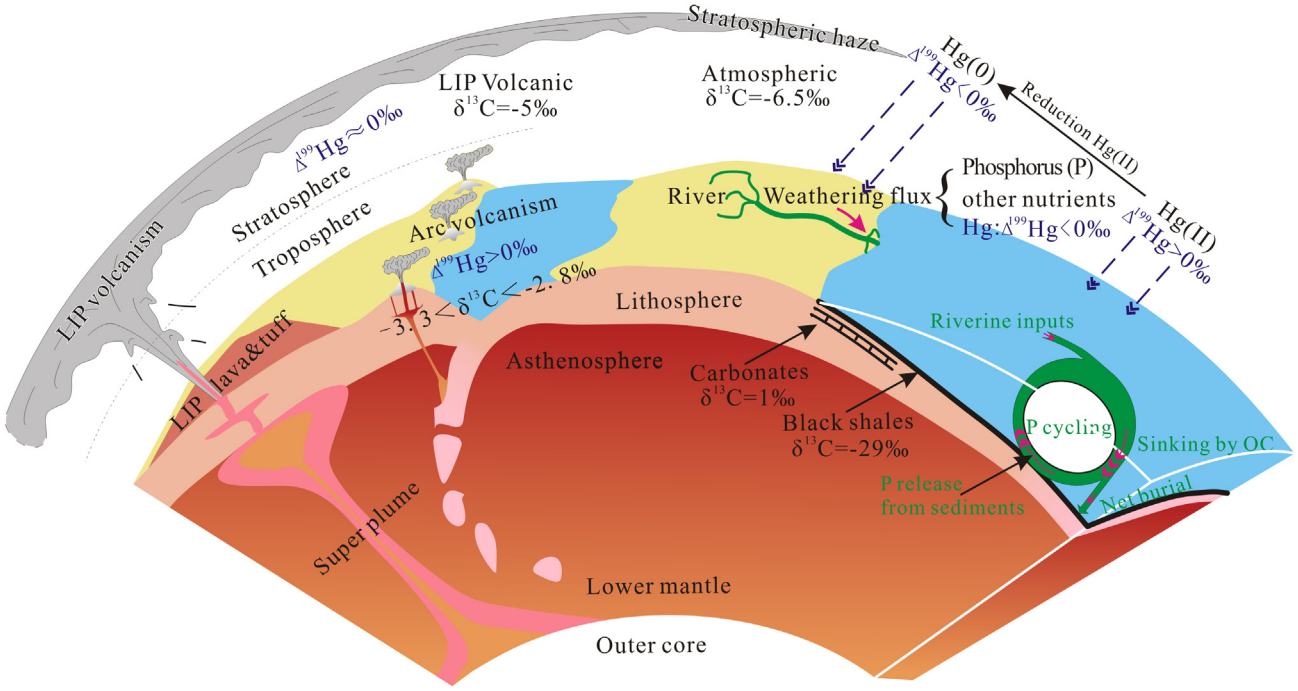

Fig. 8. Schematic diagram for stages I and III. Carbon isotopes after Mason et al. (2017), Gradstein et al. (2020), Tumiati et al. (2022); mercury isotopes after Yin et al. (2022).

ocean anoxia preceding the first pulse of LIP magmatism (Figs. 4, 6 and 7) are feasible and consistent with the environmental effects of LIP magmatism (Fig. 8).

Moreover, no positive excursion of $\delta^{13}C_{org}$ is found in our data and their correlatives in stage I (Fig. 5). The $\delta^{13}C$ of CO_2 exhaled by LIPs is commonly lower than that from arc volcanism (Mason et al., 2017; Tumiati et al., 2022) (Fig. 8). When a LIP is emplaced in the organic-carbon-rich sedimentary basin, it would expel bursts of CO_2 with even lower $\delta^{13}C$, as exemplified by the Karoo-Ferrar LIP in the Karoo Basin (Heimdal et al., 2021; Gaynor et al., 2022). Therefore, the absence of positive $\delta^{13}C_{org}$ against high productivity and thus light carbon sequestration might be additional evidence for CO_2 exhaled by LIP magmatism, rather than arc volcanoes like the Tacon Arc (Landing, 2018).

To sum up, the comprehensive stratigraphic proxy records in this study indicate that the first pulse of LIP magmatism might have initiated and sustained stage I (Figs. 6–8). The high primary productivity and thus anoxia (Shen et al., 2018) might could also benefit from enhanced continental weathering by plants (Lenton et al., 2012; Porada et al., 2016) or by tectonic drifting/collision (Kump et al., 1999; Nardin et al., 2011; Swanson-Hysell and Macdonald, 2017). However, their role should be secondary, to comply with the stratigraphic proxy records and favor the following stages of the ATOCS during the Ordovician-Silurian period.

5.3.2. Stage II without evident LIP magmatism

The high primary productivity and consequential organic carbon burial, together with the intense terrestrial weathering by LIP magmatism of stage I, could have effectively sequestered atmospheric CO_2 and drawn down pCO_2 below a critical threshold for the onset of Hirnantian glaciation. Moreover, a previous study has uncovered a temporal coincidence between LIPs and the start of global glaciations over the past 720 million years (Youbi et al., 2021). Besides CO_2 drawdown, organic carbon burial, accompanied by pyrites burial, could increase O_2 contents in the atmosphere and ocean, since they consist of the source of free oxygen (O_2) in the Earth system (Huang et al., 2021).

Notably, stage II is not a single stable period with enormous continental glaciation; instead, it consists of multiple geologically short pulses of glaciation (Page et al., 2007; Melchin et al., 2013; Li et al., 2021). It might be possible that minor pulses of LIP magmatism have the potential to cause such swift fluctuations under the background of extreme state of stage II. Further research is desired because stratigraphic proxies are currently not enough in this study due to strata condensation and permission of sampling density.

Therefore, stage II contrasts sharply with stage I on the whole (Figs. 6 and 9), and has further turbulence under the already extreme background, which would have been a period of real torture over and over again for marine life therein during the Ordovician-Silurian transition.

5.3.3. Stage III with the second pulse of LIP magmatism

Different from the high consistency of Hg and S proxies indicating the first pulse of LIP magmatism, not all reported sites have such distinct "smoking guns" in the lowermost Stage III (Fig. 7), which suggests a possible difference in the eruptive scales and/or styles. Furthermore, in contrast to the first pulse of LIP magmatism during stage I, the second pulse covers just the earliest portion of stage III (Figs. 6 and 7), which is typical of sudden deglaciation, continued eutrophication, anoxia, and the last period of LOME (Figs. 6 and 8).

The resurgence of LIP magmatism in stage III, that is, the second pulse of LIP magmatism, has the potential to cause the abrupt deglaciation of the Hirnantian glaciation due to its global warming effect (Figs. 6 and 8). Similarly, the Deccan Traps have been proposed to end the late Cretaceous global cooling (Youbi et al., 2021). Additionally, the coupled weak chemical weathering and organic carbon burial effectively slashed CO_2 sequestration during stage II (Fig. 9), favoring the accumulation of atmospheric CO_2. Nevertheless, whether such CO_2 accumulation is sufficient to cause deglaciation has yet to be explored to our knowledge.

According to all models for the LOME, mass extinction occurred only in the early portion of stage III and was succeeded with pro-

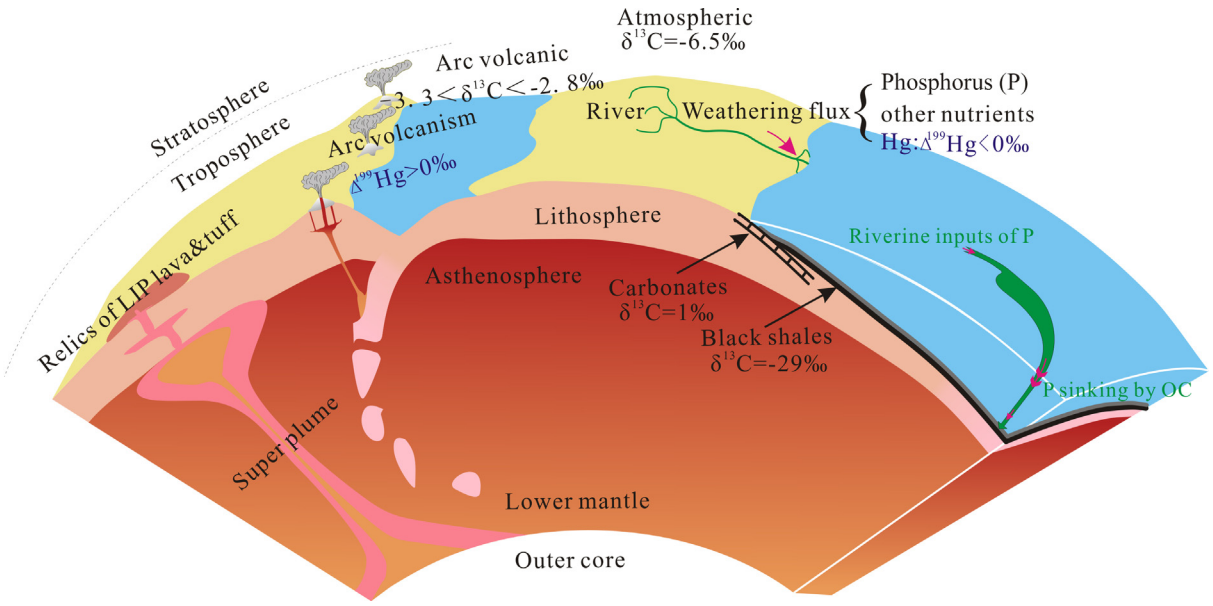

Fig. 9. Schematic diagram for stages II and IV. Carbon isotopes after Mason et al. (2017), Gradstein et al. (2020), Tumiati et al. (2022); mercury isotopes after Yin et al. (2022).

longed radiation against LIP magmatism and ocean anoxia (Rasmussen et al., 2019; Wang et al., 2019; Bond and Grasby, 2020; Fan et al., 2020; Gradstein et al., 2020; Deng et al., 2021b) (Figs. 1 and 6). Therefore, we propose that severe environmental pressure for marine life arose from the extreme ATOCS of stages I-III, and the shifts of the contrasting stages posed an even more devastating threat to marine life. After suffering the loss to a great extent during stage II and its transition to stage III, a way of coping might later be available for marine life as evidenced by the radiation in the middle and late stage III (Fig. 6).

5.3.4. Stage IV without LIP magmatism

The negative feedback of the high primary productivity and consequential organic carbon burial of stage III might be similar to those of stage I, causing global cooling and oxygenation. The widespread deposition of black shales, which preferably sequester the light carbon of the atmospheric-oceanic system (Fig. 8), might have generated the low-amplitude yet globally correlative positive $\delta^{13}C_{org}$ excursions of Stage IV (Fig. 5). However, intense glaciation and mass extinction comparable to those of stage II did not occur (Fig. 6).

Compared with the ATOCS of stage II, the less extreme conditions of stage IV might have arisen from the variation in scales and/or styles of different pulses of LIP magmatism, the lack of LIP magmatism in the latter portion of stage III, as well as lack of corresponding intense terrestrial weathering. Therefore, the contrasting ATOCSs of stages II and IV illuminated the prevailing role of LIP magmatism in driving abrupt global environmental and biological changes, and triggering and sustaining the persistent global anoxia/euxinia similar to those of stages I and III (Fig. 8).

6. Conclusions and implications

This study reports the first high-resolution, integrated geochemical record of Hg (concentrations and isotopic compositions), organic carbon isotopes ($\delta^{13}C_{org}$), and whole-rock geochemical data spanning the Ordovician-Silurian transition, from late Katian through Hirnantian to Rhuddannian Age. Based on the comprehensive analysis of stratigraphic proxy records with high-resolution graptolite zonation, we identified four successive, yet contrasting stages of the ATOCSs during the Ordovician-Silurian transition. Moreover, we propose that the two-pulse LIP magmatism are coupled with the extreme ATOCSs, each with special pCO_2, weathering rate, primary productivity, redox condition, climatic mode, and biotic evolution.

For stage I, the first pulse of LIP magmatism triggered global warming, enhanced terrestrial weathering, eutrophication, anoxia, and P recycling, leading to widespread black shales' deposition. During stage II, the Hirnantian glaciation and oxygenation arose from the intense chemical weathering and black shales' deposition of stage I. Then, in early stage III, the second pulse of LIP magmatism triggered the deglaciation and the ATOCS similar to those of stage I. Furthermore for stage IV, the black shales' deposition of stage III caused another oxygenation and positive $\delta^{13}C_{org}$ excursion.

Besides the environmental pressure caused by the peculiar states of the ATOCS in each stage, their transitions might have been more devastating in triggering the prolonged Late Ordovician mass extinction (LOME). Limited biotic recovery was possible in the later portion of stages I and III, respectively.

The multi-proxy study of continuous strata of the Silurian-Ordovician transition provides an excellent opportunity for better illuminating LIPs' essential role in driving the "roller-coaster" behavior of the ATOCS and thus profound biotic crisis during the pivotal period of the Ordovician-Silurian transition. We appeal for more future works on the ATOCS during the Ordovician-Silurian transition and other similar periods due to the various patterns of LIPs themselves and their complex interactions with the ATOCS.

CRediT authorship contribution statement

Licai Song: Conceptualization, Data curation, Funding acquisition, Investigation, Writing – original draft, Writing – review & editing. **Qing Chen:** Data curation, Formal analysis, Investigation, Methodology, Writing – original draft. **Huijun Li:** Data curation, Formal analysis, Investigation, Writing – original draft. **Changzhou Deng:** Conceptualization, Data curation, Formal analysis, Investigation, Methodology, Supervision, Writing – original draft, Writing – review & editing.

Declaration of Competing Interest

The authors declare that they have no known competing financial interests or personal relationships that could have appeared to influence the work reported in this paper.

Acknowledgments

This research was supported by the National Natural Science Foundation of China (41873047, 41372123), National Science and Technology Major Project (2016ZX05034), and Geological Survey Program of China (DD20190085). We deeply appreciate the editorial handling and the constructive comments from the anonymous reviewers. Dr. Jun Shen from China University of Geosciences was thanked for giving constructive comments.

Appendix A. Supplementary data

Supplementary data to this article can be found online at https://doi.org/10.1016/j.gsf.2023.101537.

References

Algeo, T.J., Li, C., 2020. Redox classification and calibration of redox thresholds in sedimentary systems. Geochim. Cosmochim. Acta 287, 8–26.
Algeo, T.J., Liu, J., 2020. A re-assessment of elemental proxies for paleoredox analysis. Chem. Geol. 540, 119549.
Algeo, T.J., Rowe, H., 2012. Paleoceanographic applications of trace-metal concentration data. Chem. Geol. 324–325, 6–18.
Arthur, M.A., Sageman, B.B., 1994. Marine black shales: Depositional mechanisms and environments of ancient deposits. Annu. Rev. Earth Planet. Sci. 22, 499–551.
Bartlett, R., Elrick, M., Wheeley, J.R., Polyak, V., Desrochers, A., Asmerom, Y., 2018. Abrupt global-ocean anoxia during the Late Ordovician-early Silurian detected using uranium isotopes of marine carbonates. Proc. Natl. Acad. Sci. 115, 5896–5901.
Bergquist, B., Blum, J., 2007. Mass-dependent and -independent fractionation of Hg isotopes by photoreduction in aquatic systems. Science 318, 417–420.
Bergström, S.M., Goldman, D., 2019. $\delta^{13}C$ chemostratigraphy of the Ordovician-Silurian boundary interval. In: Sial, A.N., Gaucher, C., Ramkumar, M., Ferreira, V. P. (Eds.), Chemostratigraphy Across Major Chronological Boundaries. AGU and Wiley & Sons Inc, Washington and Hoboken, pp. 143–158.
Black, B.A., Gibson, S.A., 2019. Deep carbon and the life cycle of large igneous provinces. Elements 15, 319–324.
Black, B.A., Karlstrom, L., Mather, T.A., 2021b. The life cycle of large igneous provinces. Nat. Rev. Earth Environ. 2, 840–857.
Black, B., Mittal, T., Lingo, F., Walowski, K., Hernandez, A., 2021a. Assessing the environmental consequences of the generation and alteration of mafic volcaniclastic deposits during large igneous province emplacement. In: Ernst, R.E., Dickson, A.J., Bekker, A. (Eds.), LArge Igneous Provinces: A Driver of GlobAl EnvironmentAl and Biotic ChAnges. AGU and Wiley & Sons Inc, Washington and Hoboken, pp. 117–131.
Blum, J., Bergquist, B., 2007. Reporting of variations in the natural isotopic composition of mercury. Anal. Bioanal. Chem. 388, 353–359.
Blum, J.D., Sherman, L.S., Johnson, M.W., 2014. Mercury isotopes in Earth and envirionmental sciences. Annu. Rev. Earth Planet. Sci. 42, 249–269.
Bond, D.P.G., Grasby, S.E., 2020. Late Ordovician mass extinction caused by volcanism, warming, and anoxia, not cooling and glaciation. Geology 48, 777–781.
Brand, U., Davis, A.M., Shaver, K.K., Blamey, N.J.F., Heizler, M., Lécuyer, C., 2021. Atmospheric oxygen of the Paleozoic. Earth-Sci. Rev. 216, 103560.
Braun, M.G., Daoust, P., Desrochers, A., 2021. A sequential record of the Llandovery $\delta^{13}C_{carb}$ excursions paired with time-specific facies: Anticosti Island, eastern Canada. Palaeogeogr. Palaeoclimatol. Palaeoecol. 578, 110566.
Brenchley, P.J., Marshall, J.D., Harper, D.A.T., Buttler, C.J., Underwood, C.J., 2006. A late Ordovician (Hirnantian) karstic surface in a submarine channel, recording glacio-eustatic sea-level changes: Meifod, central Wales. Geol. J. 41, 1–22.
Calner, M., Bockelie, J., Rasmussen, C., Calner, H., Lehnert, O., Joachimski, M., 2021. Carbon isotope chemostratigraphy and sea- level history of the Hirnantian Stage (uppermost Ordovician) in the Oslo-Asker district, Norway. Geol. Mag. 158, 1977–2008.
Chen, X., Rong, J.-Y., Li, Y., Boucot, A.J., 2004. Facies patterns and geography of the Yangtze region, South China, through the Ordovician and Silurian transition. Palaeogeogr. Palaeoclimatol. Palaeoecol. 204, 353–372.
Chen, X., Fan, J., Zhang, Y., Wang, H., Chen, Q., Wang, W., Liang, F., Guo, W., Zhao, Q., Nie, H., Wen, Z., Sun, Z., 2015. Subdivision and delineation of the Wufeng and Lungmachi black shales in the subsurface areas of the Yangtze Platform. J. Strat. 39, 351–358.
Chen, X., Zhang, Y., Goldman, D., Bergström, S.M., Fan, J., Wang, Z., Finney, S.C., Chen, Q., Ma, X., 2017. Darriwilian to Katian (Ordovician) Graptolites from Northwest China. Elsevier Inc., Amsterdam, p. 354.
Chen, X., Romaniello, S.J., McCormick, M., Sherry, A., Havig, J.R., Zheng, W., Anbar, A. D., 2021. Anoxic depositional overprinting of $^{238}U/^{235}U$ in calcite: When do carbonates tell black shale tales? Geology 49, 1193–1197.
Cho, D.-L., Lee, S.R., Koh, H.J., Park, J.-B., Armstrong, R., Choi, D.K., 2014. Late Ordovician volcanism in Korea constrains the timing for breakup of Sino-Korean Craton from Gondwana. J. Asian Earth Sci. 96, 279–286.
Dahl, T.W., Hammarlund, E.U., Rasmussen, C.M.Ø., Bond, D.P.G., Canfield, D.E., 2021. Sulfidic anoxia in the oceans during the Late Ordovician mass extinctions - insights from molybdenum and uranium isotopic global redox proxies. Earth-Sci. Rev. 220, 103748.
Delabroye, A., Vecoli, M., 2010. The end-Ordovician glaciation and the Hirnantian Stage: A global review and questions about Late Ordovician event stratigraphy. Earth-Sci. Rev. 98, 269–282.
Deng, Y., Fan, J., Zhang, S., Fang, X., Chen, Z., Shi, Y., Wang, H., Wang, X., Yang, J., Hou, X., Wang, Y., Zhang, Y., Chen, Q., Yang, A., Fan, R., Dong, S., Xu, H., Shen, S., 2021b. Timing and patterns of the Great Ordovician Biodiversification Event and Late Ordovician mass extinction: Perspectives from South China. Earth-Sci. Rev. 220, 103743.
Deng, C.Z., Lehmann, B., Xiao, T.T., Tan, Q.P., Chen, D., Tian, Z.D., Wang, X.Y., Sun, G. Y., Yin, R.S., 2022. Intracontinental and arc-related hydrothermal systems display distinct $\delta^{202}Hg$ and $\Delta^{199}Hg$ features: Implication for large-scale mercury recycling and isotopic fractionation in different tectonic settings. Earth Planet. Sci. Lett. 593, 117646.
Deng, C., Sun, G., Rong, Y., Sun, R., Sun, D., Lehmann, B., Yin, R., 2021a. Recycling of mercury from the atmosphere-ocean system into volcanic-arc-associated epithermal gold systems. Geology 49, 309–313.
Derakhshi, M., Ernst, R.E., Kamo, S.L., 2022. Ordovician-Silurian volcanism in northern Iran: Implications for a new Large Igneous Province (LIP) and a robust candidate for the Late Ordovician mass extinction. Gondwana Res. 107, 256–280.
Du, X., Jia, J., Zhao, K., Shi, J., Shu, Y., Liu, Z., Duan, D., 2021. Was the volcanism during the Ordovician-Silurian transition in South China actually global in extent? Evidence from the distribution of volcanic ash beds in black shales. Mar. Petrol. Geol. 123, 104721.
Edwards, C.T., Saltzman, M.R., 2016. Paired carbon isotopic analysis of Ordovician bulk carbonate ($\delta^{13}C_{carb}$) and organic matter ($\delta^{13}C_{org}$) spanning the Great Ordovician Biodiversification Event. Palaeogeogr. Palaeoclimatol. Palaeoecol. 458, 102–117.
Ernst, R.E., Bond, D.P.G., Zhang, S.H., Buchan, K.L., Grasby, S.E., Youbi, N., El Bilali, H., Bekker, A., Doucet, L.S., 2021. Large igneous province record through time and implications for secular environmental changes and geological time-scale boundaries. In: Ernst, R.E., Dickson, A.J., Bekker, A. (Eds.), LArge Igneous Provinces: A Driver of GlobAl EnvironmentAl and Biotic ChAnges. AGU and Wiley & Sons Inc, Washington and Hoboken, pp. 3–26.
Fan, J., Peng, P.A., Melchin, M.J., 2009. Carbon isotopes and event stratigraphy near the Ordovician-Silurian boundary, Yichang, South China. Palaeogeogr. Palaeoclimatol. Palaeoecol. 276, 160–169.
Fan, J., Shen, S., Erwin, D., Sadler, P., MacLeod, N., Cheng, Q.-M., Hou, X.-D., Yang, J., Wang, X.-D., Wang, Y., Zhang, H., Chen, X., Li, G.-X., Zhang, Y., Shi, Y.-K., Yuan, D., Chen, Q., Zhang, L.-N., Li, C., Zhao, Y.-Y., 2020. A high-resolution summary of Cambrian to Early Triassic marine invertebrate biodiversity. Science 367, 272–277.
Finnegan, S., Bergmann, K., Eiler, J.M., Jones, D.S., Fike, D.A., Eisenman, I., Hughes, N. C., Tripati, A.K., Fischer, W.W., 2011. The magnitude and duration of Late Ordovician-Early Silurian glaciation. Science 331, 903–906.
Finney, S.C., Berry, W.B.N., Cooper, J.D., Ripperdan, R.L., Sweet, W.C., Jacobson, S.R., Soufiane, A., Achab, A., Noble, P.J., 1999. Late Ordovician mass extinction: A new perspective from stratigraphic sections in central Nevada. Geology 27, 215–218.
Fox, C.P., Whiteside, J.H., Olsen, P.E., Cui, X., Summons, R.E., Idiz, E., Grice, K., 2022. Two-pronged kill mechanism at the end-Triassic mass extinction. Geology 50, 448–453.
Gaynor, S.P., Svensen, H.H., Polteau, S., Schaltegger, U., 2022. Local melt contamination and global climate impact: Dating the emplacement of Karoo LIP sills into organic-rich shale. Earth Planet. Sci. Lett. 579, 117371.
Gelman, F., Binstock, R., Halicz, L., 2012. Application of the Walkley-Black titration for the organic carbon quantification in organic rich sedimentary rocks. Fuel 96, 608–610.
Ghienne, J.-F., Desrochers, A., Vandenbroucke, T.R.A., Achab, A., Asselin, E., Dabard, M.-P., Farley, C., Loi, A., Paris, F., Wickson, S., Veizer, J., 2014. A Cenozoic-style scenario for the end-Ordovician glaciation. Nat. Commun. 5, 4485.
Gibbs, M., Barron, E., Kump, L., 1997. An atmospheric pCO_2 threshold for glaciation in the Late Ordovician. Geology 25, 447–450.
Goldberg, S.L., Present, T.M., Finnegan, S., Bergmanna, K.D., 2021. A high-resolution record of early Paleozoic climate. Sci. Adv. 118, e2013.
Gong, Q., Wang, X., Zhao, L., Grasby, S., Chen, Z.-Q., Zhang, L., Li, Y., Cao, L., Li, Z., 2017. Mercury spikes suggest volcanic driver of the Ordovician-Silurian mass extinction. Sci. Rep. 7, 5304.
Gradstein, F.M., Ogg, J.G., Schmitz, M.D., Ogg, G.M., 2020. Geological Time Scale 2020. Elsevier Inc., Amsterdam, p. 1280.
Grasby, S.E., Them, T.R., Chen, Z., Yin, R., Ardakani, O.H., 2019. Mercury as a proxy for volcanic emissions in the geologic record. Earth-Sci. Rev. 196, 102880.
Grasby, S.E., Liu, X., Yin, R., Ernst, R.E., Chen, Z., 2020. Toxic mercury pulses into late Permian terrestrial and marine environments. Geology 48, 830–833.

Gu, X., Zhang, L., Yin, R., Grasby, S.E., Yao, H., Tan, J., Wang, C., 2022. Deccan volcanic activity and its links to the end-Cretaceous extinction in northern China. Glob. Planet. Chang. 210, 103772.
Hammarlund, E.U., Dahl, T.W., Harper, D.A.T., Bond, D.P.G., Nielsen, A.T., Bjerrum, C. J., Schovsbo, N.H., Schönlaub, H.P., Zalasiewicz, J.A., Canfield, D.E., 2012. A sulfidic driver for the end-Ordovician mass extinction. Earth Planet. Sci. Lett. 331–332, 128–139.
Hammarlund, E.U., Loydell, D.K., Nielsen, A.T., Schovsbo, N.H., 2019. Early Silurian $\delta^{13}C_{org}$ excursions in the foreland basin of Baltica, both familiar and surprising. Palaeogeogr. Palaeoclimatol. Palaeoecol. 526, 126–135.
Harper, D.A.T., Hammarlund, E.U., Rasmussen, C.M.Ø., 2014. End Ordovician extinctions: A coincidence of causes. Gondwana Res. 25, 1294–1307.
Harper, D.A.T., Cascales-Miñana, B., Servais, T., 2020. Early Palaeozoic diversifications and extinctions in the marine biosphere: a continuum of change. Geol. Mag. 157, 5–21.
Hartmann, J., Moosdorf, N., Lauerwald, R., Hinderer, M., West, A.J., 2014. Global chemical weathering and associated P-release - The role of lithology, temperature and soil properties. Chem. Geol. 363, 145–163.
Heimdal, T.H., Godderis, Y., Jones, M.T., Svensen, H.H., 2021. Assessing the importance of thermogenic degassing from the Karoo Large Igneous Province (LIP) in driving Toarcian carbon cycle perturbations. Nat. Commun. 12, 6221.
Herrmann, A., Patzkowsky, M., Pollard, D., 2003. Obliquity forcing with 8–12 times preindustrial levels of atmospheric pCO_2 during the Late Ordovician glaciation. Geology 31, 485–488.
Horton, F., 2015. Did phosphorus derived from the weathering of large igneous provinces fertilize the Neoproterozoic ocean? Geochem. Geophys. Geosyst. 16, 1723–1738.
Hu, D., Li, M., Zhang, X., Turchyn, A.V., Gong, Y., Shen, Y., 2020. Large mass-independent sulphur isotope anomalies link stratospheric volcanism to the Late Ordovician mass extinction. Nat. Commun. 11, 2297.
Hu, D., Li, M., Chen, J., Luo, Q., Grasby, S.E., Zhang, T., Yuan, S., Xu, Y., Finney, S.C., Sun, L., Shen, Y., 2021. Major volcanic eruptions linked to the Late Ordovician mass extinction: Evidence from mercury enrichment and Hg isotopes. Glob. Planet. Chang. 196, 103374.
Huang, J., Liu, X., He, Y., Shen, S., Hou, Z., Li, S., Li, C., Yao, L., Huang, J., 2021. The oxygen cycle and a habitable Earth. Sci. China Earth Sci. 64, 511–528.
Hull, P.M., Bornemann, A., Penman, D.E., Henehan, M.J., Norris, R.D., Wilson, P.A., Blum, P., Alegret, L., Batenburg, S.J., Bown, P.R., Bralower, T.J., Cournede, C., Deutsch, A., Donner, B., Friedrich, O., Jehle, S., Kim, H., Kroon, D., Lippert, P.C., Loroch, D., Moebius, I., Moriya, K., Peppe, D.J., Ravizza, G.E., Röhl, U., Schueth, J. D., Sepúlveda, J., Sexton, P.F., Sibert, E.C., Śliwińska, K.K., Summons, R.E., Thomas, E., Westerhold, T., Whiteside, J.H., Yamaguchi, T., Zachos, J.C., 2020. On impact and volcanism across the Cretaceous-Paleogene boundary. Science 367, 266–272.
Jenkyns, H.C., 2010. Geochemistry of oceanic anoxic events. Geochem. Geophys. Geosyst. 11, 002788.
Jones, D.S., Martini, A.M., Fike, D.A., Kaiho, K., 2017. A volcanic trigger for the Late Ordovician mass extinction? Mercury data from south China and Laurentia. Geology 45, 631–634.
Kasbohm, J., 2022. Flood basalt buildup warms climate. Nat. Geosci. 15, 342–343.
Kasbohm, J., Schoene, B., Burgess, S., 2021. Radiometric constraints on the timing, tempo, and effects of large igneous province emplacement. In: Ernst, R.E., Dickson, A.J., Bekker, A. (Eds.), LArge Igneous Provinces: A Driver of GlobAl EnvironmentAl and Biotic ChAnges. AGU and Wiley & Sons Inc, Washington and Hoboken, pp. 27–82.
Khudoley, A.K., Prokopiev, A.V., Chamberlain, K.R., Savelev, A.D., Ernst, R.E., Malyshev, S.V., Moskalenko, A.N., Lebedeva, O.Y., 2020. Late Ordovician mafic magmatic event, southeast Siberia: Tectonic implications, LIP interpretation, and potential link with a mass extinction. Minerals 10, 1108.
Klemme, H.D., Ulmishek, G.F., 1991. Effective petroleum source rocks of the world: stratigraphic distribution and controlling depositional factors. AAPG Bull. 75, 1809–1851.
Kröger, B., Franeck, F., Rasmussen, C.M.Ø., 2019. The evolutionary dynamics of the early Palaeozoic marine biodiversity accumulation. Proc. R. Soc. B 286, 20191634.
Kump, L., Arthur, M., Patzkowsky, M.E., Gibbs, M.T., Pinkus, D.S., Sheehan, P., 1999. A weathering hypothesis for glaciation at high atmospheric pCO_2 during the Late Ordovician. Palaeogeogr. Palaeoclimatol. Palaeoecol. 152, 173–187.
Kump, L.R., Arthur, M.A., 1999. Interpreting carbon-isotope excursions: carbonates and organic matter. Chem. Geol. 161, 181–198.
Kump, L.R., Brantley, S.L., Arthur, M.A., 2000. Chemical weathering, atmospheric CO_2, and climate. Annu. Rev. Earth Planet. Sci. 28, 611–667.
Landing, E., 2018. Tropical weathering of the Taconic orogeny (i.e., "orogen") as a driver for Ordovician cooling. Geology 46, e436.
Lefebvre, V., Servais, T., François, L., Averbuch, O., 2010. Did a Katian large igneous province trigger the Late Ordovician glaciation? Palaeogeogr. Palaeoclimatol. Palaeoecol. 296, 310–319.
Lenton, T.M., Crouch, M., Johnson, M., Pires, N., Dolan, L., 2012. First plants cooled the Ordovician. Nat. Geosci. 5, 86–89.
Lenton, T.M., Daines, S.J., Mills, B.J.W., 2018. COPSE reloaded: An improved model of biogeochemical cycling over Phanerozoic time. Earth-Sci. Rev. 178, 1–28.
Li, C., Zhang, J., Li, W., Botting, J., Chen, Q., Fan, J., Zhang, Y., 2021. Multiple glacio-eustatic cycles and associated environmental changes through the Hirnantian (Late Ordovician) in South China. Glob. Planet. Chang. 207, 103668.
Lindström, S., Sanei, H., van de Schootbrugge, B., Pedersen, G., Lesher, C., Tegner, C., Heunisch, C., Dybkjaer, K., Outridge, P.M., 2019. Volcanic mercury and mutagenesis in land plants during the end-Triassic mass extinction. Sci. Adv. 5, eaaw4018.
Liu, M., Chen, D., Jiang, L., Stockey, R.G., Aseal, D., Zhang, B., Liu, K., Yang, X., Yan, D., Planavsky, N.J., 2022. Oceanic anoxia and extinction in the latest Ordovician. Earth Planet. Sci. Lett. 588, 117553.
Lu, Y., Shen, J., Wang, Y., Lu, Y., Algeo, T.J., Jiang, S., Yan, D., Gou, Q., 2022. Seawater sources of Hg enrichment in Ordovician-Silurian boundary strata, South China. Palaeogeogr. Palaeoclimatol. Palaeoecol. 601, 111156.
Ma, Y., Cai, X., Zhao, P., 2018. China's shale gas exploration and development: Understanding and practice. Petrol. Explor. Develop. 45, 589–603.
Männik, P., Lehnert, O., Nõlvak, J., Joachimski, M.M., 2021. Climate changes in the pre-Hirnantian Late Ordovician based on $\delta^{18}O_{phos}$ studies from Estonia. Palaeogeogr. Palaeoclimatol. Palaeoecol. 569, 110347.
Marcilly, C.M., Maffre, P., Le Hir, G., Pohl, A., Fluteau, F., Goddéris, Y., Donnadieu, Y., Heimdal, H.T., Torsvik, T.H., 2022. Understanding the early Paleozoic carbon cycle balance and climate change from modelling. Earth Planet. Sci. Lett. 594, 117717.
Mason, E., Edmonds, M., Turchyn, A.V., 2017. Remobilization of crustal carbon may dominate volcanic arc emissions. Science 357, 290–294.
McKenzie, N.R., Jiang, H., 2019. Earth's outgassing and climatic transitions: the slow burn towards environmental "Catastrophes"? Elements 15, 325–330.
Melchin, M.J., Holmden, C., 2006a. Carbon isotope chemostratigraphy in Arctic Canada: Sea-level forcing of carbonate platform weathering and implications for Hirnantian global correlation. Palaeogeogr. Palaeoclimatol. Palaeoecol. 234, 186–200.
Melchin, M.J., Holmden, C., 2006b. Carbon isotope chemostratigraphy of the Llandovery in Arctic Canada: Implications for global correlation and sea-level change. GFF 128, 173–180.
Melchin, M.J., Mitchell, C.E., Holmden, C., Storch, P., 2013. Environmental changes in the Late Ordovician-early Silurian: Review and new insights from black shales and nitrogen isotopes. GSA. Bull. 125, 1635–1670.
Meyer, K.M., Kump, L.R., 2008. Oceanic euxinia in earth history: Causes and consequences. Annu. Rev. Earth Planet. Sci. 36, 251–288.
Nardin, E., Godderis, Y., Donnadieu, Y., Hir, G.L., Blakey, R.C., Puceat, E., Aretz, M., 2011. Modeling the early Paleozoic long-term climatic trend. GSA. Bull. 123, 1181–1192.
Nauter-Alves, A., 2022. Tracing past volcanic activity with sedimentary Hg concentrations. Nat. Rev. Earth Environ. 3, 554.
Nava, A., Black, B., Gibson, S., Bodnar, R., Renne, P., Vanderkluysen, L., 2021. Reconciling early Deccan Traps CO_2 outgassing and pre-KPB global climate. Proc. Natl. Acad. Sci. 118, e2007.
Page, A.A., Zalasiewicz, J.A., Williams, M., Popov, L.E., 2007. Were transgressive black shales a negative feedback modulating glacioeustasy in the Early Palaeozoic icehouse? In: Williams, M., Haywood, A.M., Gregory, F.J., Schmidt, D.N. (Eds.), Deep-time Perspectives on Climate Change: Marrying the Signal From Computer Models and Biological Proxies. Geol. Soc. Pub, House, Bath, pp. 123–156.
Papadomanolaki, N.M., Lenstra, W.K., Wolthers, M., Slomp, C.P., 2022. Enhanced phosphorus recycling during past oceanic anoxia amplified by low rates of apatite authigenesis. Sci. Adv. 8, eabn2370.
Pasquier, V., Bryant, R.N., Fike, D.A., Halevy, I., 2021. Strong local, not global, controls on marine pyrite sulfur isotopes. Sci. Adv. 7, eabb7403.
Pasquier, V., Fike, D.A., Révillon, S., Halevy, I., 2022. A global reassessment of the controls on iron speciation in modern sediments and sedimentary rocks: A dominant role for diagenesis. Geochim. Cosmochim. Acta 335, 211–230.
Penman, D.E., Caves Rugenstein, J.K., Ibarra, D.E., Winnick, M.J., 2020. Silicate weathering as a feedback and forcing in Earth's climate and carbon cycle. Earth-Sci. Rev. 209, 103298.
Percival, L.M.E., Bergquist, B.A., Mather, T.A., Sanei, H., 2021. Sedimentary mercury enrichments as a tracer of large igneous province volcanism. In: Ernst, R.E., Dickson, A.J., Bekker, A. (Eds.), LArge Igneous Provinces: A Driver of GlobAl EnvironmentAl and Biotic ChAnges. AGU and Wiley & Sons Inc, Washington and Hoboken, pp. 247–262.
Piper, D.Z., Calvert, S.E., 2009. A marine biogeochemical perspective on black shale deposition. Earth-Sci. Rev. 95, 63–96.
Pogge von Strandmann, P.A.E., Desrochers, A., Murphy, M.J., Finlay, A.J., Selby, D., Lenton, T.M., 2017. Global climate stabilisation by chemical weathering during the Hirnantian glaciation. Geochem. Perspect. Lett. 3, 230–237.
Pohl, A., Donnadieu, Y., Hir, G., Ladant, J.-B., Dumas, C., Alvarez-Solas, J., Vandenbroucke, T., 2016. Glacial onset predated Late Ordovician climate cooling. Paleoceanography 31, 800–821.
Pohl, A., Lu, Z., Lu, W., Stockey, R.G., Elrick, M., Li, M., Desrochers, A., Shen, Y., He, R., Finnegan, S., Ridgwell, A., 2021. Vertical decoupling in Late Ordovician anoxia due to reorganization of ocean circulation. Nat. Geosci. 14, 868–873.
Pope, M.C., Steffen, J.B., 2003. Widespread, prolonged late Middle to Late Ordovician upwelling. Geology 31, 63–66.
Porada, P., Lenton, T.M., Pohl, A., Weber, B., Mander, L., Donnadieu, Y., Beer, C., Poschl, U., Kleidon, A., 2016. High potential for weathering and climate effects of non-vascular vegetation in the Late Ordovician. Nat. Commun. 7, 12113.
Porębski, S.J., Anczkiewicz, R., Paszkowski, M., Skompski, S., Kędzior, A., Mazur, S., Szczepański, J., Buniak, A., Mikołajewski, Z., 2019. Hirnantian icebergs in the subtropical shelf of Baltica: Evidence from sedimentology and detrital zircon provenance. Geology 47, 284–288.
Qi, H., Coplen, T.B., Geilmann, H., Brand, W.A., Bohlke, J.K., 2003. Two new organic reference materials for delta ^{13}C and delta ^{15}N measurements and a new value for the delta ^{13}C of NBS 22 oil. Rapid Commun. Mass Spectrom. 17, 2483–2487.

Racki, G., 2020. Volcanism as a prime cause of mass extinctions: Retrospectives and perspectives. In: Adatte, T., Bond, D.P.G., Keller, G. (Eds.), Mass Extinctions, Volcanism, and Impacts: New Developments. GSA Inc., Boulder, pp. 1–34.
Raiswell, R., Hardisty, D.S., Lyons, T.W., Canfield, D.E., Owens, J.D., Planavsky, N.J., Poulton, S.W., Reinhard, C.T., 2018. The iron paleoredox proxies: A guide to the pitfalls, problems and proper practice. Am. J. Sci. 318, 491.
Rasmussen, C., Kröger, B., Nielsen, M., Colmenar, J., 2019. Cascading trend of Early Paleozoic marine radiations paused by Late Ordovician extinctions. Proc. Natl. Acad. Sci. 116, 7207–7213.
Rong, J., Harper, D.A.T., Huang, B., Li, R., Zhang, X., Chen, D., 2020. The latest Ordovician Hirnantian brachiopod faunas: New global insights. Earth-Sci. Rev. 208, 103280.
Saltzman, M.R., Young, S.A., 2005. Long-lived glaciation in the Late Ordovician? Isotopic and sequence-stratigraphic evidence from western Laurentia. Geology 33, 109–112.
Sanei, H., Grasby, S., Beauchamp, B., 2012. Latest Permian mercury anomalies. Geology 40, 63–66.
Schimmelmann, A., Qi, H., Coplen, T.B., Brand, W.A., Fong, J., Meier-Augenstein, W., Kemp, H.F., Toman, B., Ackermann, A., Assonov, S., Aerts-Bijma, A.T., Brejcha, R., Chikaraishi, Y., Darwish, T., Elsner, M., Gehre, M., Geilmann, H., Groning, M., Helie, J.F., Herrero-Martin, S., Meijer, H.A., Sauer, P.E., Sessions, A.L., Werner, R. A., 2016. Organic reference materials for hydrogen, carbon, and nitrogen stable isotope-ratio measurements: Caffeines, *n*-alkanes, fatty acid methyl esters, glycines, l-valines, polyethylenes, and oils. Anal. Chem. 88, 4294–4302.
Schobben, M., van de Schootbrugge, B., Wignall, P.B., 2019. Interpreting the carbon isotope record of mass extinctions. Elements 15, 331–337.
Schobben, M., Foster, W., Sleveland, A.R.N., Zuchuat, V., Svensen, H., Planke, S., Bond, D.P.G., Marcelis, F., Newton, R., Wignall, P.B., Poulton, S., 2020. A nutrient control on marine anoxia during the end-Permian mass extinction. Nat. Geosci. 13, 640–646.
Scotese, C.R., 2021. An atlas of Phanerozoic paleogeographic maps: The seas come in and the seas go out. Annu. Rev. Earth Planet. Sci. 49, 679–728.
Scotese, C.R., Song, H., Mills, B.J.W., van der Meer, D.G., 2021. Phanerozoic paleotemperatures: The Earth's changing climate during the last 540 million years. Earth-Sci. Rev. 215, 103503.
Sheehan, P.M., 2001. The Late Ordovician mass extinction. Annu. Rev. Earth Planet. Sci. 29, 331–364.
Shen, J., Pearson, A., Henkes, G., Zhang, Y., Chen, K., Li, D., Wankel, S., Finney, S., Shen, Y., 2018. Improved efficiency of the biological pump as a trigger for the Late Ordovician glaciation. Nat. Geosci. 11, 510–514.
Shen, J., Algeo, T.J., Chen, J., Planavsky, N.J., Feng, Q., Yu, J., Liu, J., 2019. Mercury in marine Ordovician/Silurian boundary sections of South China is sulfide-hosted and non-volcanic in origin. Earth Planet. Sci. Lett. 511, 130–140.
Shen, J., Algeo, T.J., Feng, Q., 2022a. Mercury isotope evidence for a non-volcanic origin of Hg spikes at the Ordovician-Silurian boundary, South China. Earth Planet. Sci. Lett. 594, 117705.
Shen, J., Yin, R., Zhang, S., Algeo, T.J., Bottjer, D.J., Yu, J., Xu, G., Penman, D., Wang, Y., Li, L., Shi, X., Planavsky, N.J., Feng, Q., Xie, S., 2022b. Intensified continental chemical weathering and carbon-cycle perturbations linked to volcanism during the Triassic-Jurassic transition. Nat. Commun. 13, 299.
Smolarek-Lach, J., Marynowski, L., Trela, W., Wignall, P.B., 2019. Mercury spikes indicate a volcanic trigger for the Late Ordovician mass extinction event: An example from a deep shelf of the peri-Baltic region. Sci. Rep. 9, 3139.
Stockey, R.G., Cole, D.B., Planavsky, N.J., Loydell, D.K., Fryda, J., Sperling, E.A., 2020. Persistent global marine euxinia in the early Silurian. Nat. Commun. 11, 1804.
Štorch, P., Manda, Š., Tasáryová, Z., Frýda, J., Chadimová, L., Melchin, M.J., 2018. A proposed new global stratotype for Aeronian Stage of the Silurian System: Hlásná Třebaň section, Czech Republic. Lethaia 51, 357–388.
Su, W., Huff, W.D., Ettensohn, F.R., Liu, X., Zhang, J.E., Li, Z., 2009. K-bentonite, black-shale and flysch successions at the Ordovician-Silurian transition, South China: Possible sedimentary responses to the accretion of Cathaysia to the Yangtze Block and its implications for the evolution of Gondwana. Gondwana Res. 15, 111–130.
Swanson-Hysell, N.L., Macdonald, F.A., 2017. Tropical weathering of the Taconic orogeny as a driver for Ordovician cooling. Geology 45, 719–722.
Taylor, S.R., McLennan, S.M., 1985. The Continental Crust: Its Composition and Evolution. Blackwell Sci. Pub, Oxford, p. 312.
Thibodeau, A.M., Ritterbush, K., Yager, J.A., West, A.J., Ibarra, Y., Bottjer, D.J., Berelson, W.M., Bergquist, B.A., Corsetti, F.A., 2016. Mercury anomalies and the timing of biotic recovery following the end-Triassic mass extinction. Nat. Commun. 7, 11147.
Tian, X., Buck, W.R., 2022. Intrusions induce global warming before continental flood basalt volcanism. Nat. Geosci. 15, 417–422.
Torsvik, T.H., Svensen, H.H., Steinberger, B., Royer, D.L., Jerram, D.A., Jones, M.T., Domeier, M., 2021. Connecting the deep Earth and the atmosphere. In: Marquardt, H., Ballmer, M., Cottaar, S., Konter, J. (Eds.), Mantle Convection and Surface Expressions. AGU and Wiley & Sons Inc, Washington and Hoboken, pp. 413–453.
Trela, W., Podhalańska, T., Smolarek, J., Marynowski, L., 2016. Llandovery green/grey and black mudrock facies of the northern Holy Cross Mountains (Poland) and their relation to early Silurian sea-level changes and benthic oxygen level. Sediment. Geol. 342, 66–77.
Tribovillard, N., 2021. Re-assessing copper and nickel enrichments as paleo-productivity proxies. BSGF - Earth Sci. Bull. 200047, 20121.
Tribovillard, N., Algeo, T.J., Lyons, T., Riboulleau, A., 2006. Trace metals as paleoredox and paleoproductivity proxies: An update. Chem. Geol. 232, 12–32.
Trotter, J.A., Williams, I.S., Barnes, C.R., Lecuyer, C., Nicoll, R.S., 2008. Did cooling oceans trigger Ordovician biodiversification? Evidence from conodont thermometry. Science 321, 550–554.
Tumiati, S., Recchia, S., Remusat, L., Tiraboschi, C., Sverjensky, D.A., Manning, C.E., Vitale Brovarone, A., Boutier, A., Spanu, D., Poli, S., 2022. Subducted organic matter buffered by marine carbonate rules the carbon isotopic signature of arc emissions. Nat. Commun. 13, 2909.
Underwood, C.J., Crowley, S.F., Marshall, J.D., Brenchley, P.J., 1997. High-resolution carbon isotope stratigraphy of the basal Silurian Stratotype (Dob's Linn, Scotland) and its global correlation. J. Geol. Soc. 154, 709–718.
Wang, G., Zhan, R., Percival, I.G., 2019. The end-Ordovician mass extinction: A single-pulse event? Earth-Sci. Rev. 192, 15–33.
Yager, J.A., West, A.J., Thibodeau, A.M., Corsetti, F.A., Rigo, M., Berelson, W.M., Bottjer, D.J., Greene, S.E., Ibarra, Y., Jadoul, F., Ritterbush, K.A., Rollins, N., Rosas, S., Di Stefano, P., Sulca, D., Todaro, S., Wynn, P., Zimmermann, L., Bergquist, B.A., 2021. Mercury contents and isotope ratios from diverse depositional environments across the Triassic-Jurassic boundary: Towards a more robust mercury proxy for large igneous province magmatism. Earth-Sci. Rev. 223, 103775.
Yan, D., Chen, D., Wang, Q., Wang, J., 2010. Large-scale climatic fluctuations in the latest Ordovician on the Yangtze block, south China. Geology 38, 599–602.
Yang, S., Hu, W., Wang, X., Jiang, B., Yao, S., Sun, F., Huang, Z., Zhu, F., 2019. Duration, evolution, and implications of volcanic activity across the Ordovician-Silurian transition in the Lower Yangtze region, South China. Earth Planet. Sci. Lett. 518, 13–25.
Yin, R., Feng, X., Hurley, J.P., Krabbenhoft, D.P., Lepak, R.F., Kang, S., Yang, H., Li, X., 2016. Historical records of mercury stable isotopes in sediments of Tibetan lakes. Sci. Rep. 6, 23332.
Yin, R., Chen, D., Pan, X., Deng, C., Chen, L., Song, X., Yu, S., Zhu, C., Wei, X., Xu, Y., Feng, X., Blum, J.D., Lehmann, B., 2022. Mantle Hg isotopic heterogeneity and evidence of oceanic Hg recycling into the mantle. Nat. Commun. 13, 948.
Youbi, N., Ernst, R.E., Mitchell, R.N., Boumehdi, M.A., El Moume, W., Lahna, A.A., Bensalah, M.K., Söderlund, U., Doblas, M., Tassinari, C.C.G., 2021. Preliminary appraisal of a correlation between glaciations and large igneous provinces over the past 720 million years. In: Ernst, R.E., Dickson, A.J., Bekker, A. (Eds.), LArge Igneous Provinces: A Driver of GlobAl EnvironmentAl and Biotic ChAnges. AGU and Wiley & Sons Inc, Washington and Hoboken, pp. 169–190.
Zhang, L., Fan, J., Chen, Q., 2016. Geographic distribution and palaeogeographic reconstruction of the Upper Ordovician Kuanyinqiao Bed in South China. Chin. Sci. Bull. 61, 2053–2063.
Zhang, J., Lyons, T.W., Li, C., Fang, X., Chen, Q., Botting, J., Zhang, Y., 2022. What triggered the Late Ordovician mass extinction (LOME)? Perspectives from geobiology and biogeochemical modeling. Glob. Planet. Chang. 216, 103917.
Zhang, Y., Tang, P., Jin, J., Sun, S., Zhang, X., Huang, P., Sun, J., Wang, Y., 2021. Climate change in the subtropical Paleo-Tethys before the late Ordovician glaciation. Glob. Planet. Chang. 199, 103432.
Zhao, K., Du, X., Lu, Y., Hao, F., Liu, Z., Jia, J., 2020. Is volcanic ash responsible for the enrichment of organic carbon in shales? Quantitative characterization of organic-rich shale at the Ordovician-Silurian transition. GSA Bull. 133, 837–848.
Zou, C., Qiu, Z., Poulton, S., Dong, D., Wang, H., Chen, D., Lu, B., Shi, Z., Tao, H., 2018. Ocean euxinia and climate change double whammy drove the Late Ordovician mass extinction. Geology 46, 535–538.